IOP Publishing Journal of Physics D: Applied Physics

J. Phys. D: Appl. Phys. **47** (2014) 405206 (24pp) doi:10.1088/0022-3727/47/40/405206

Effect of turbulence modulation on three-dimensional trajectories of powder particles in a plasma spray process

S Shang[1], B Guduri[1], M Cybulsky[2] and R C Batra[1,3,4]

[1] Department of Biomedical Engineering and Mechanics, M/C 0219, Virginia Polytechnic Institute and State University, Blacksburg, VA 24061, USA
[2] Rolls-Royce Corporation, PO Box 420, Speed Code W-08, Indianapolis, IN 46206-0420, USA
[3] Rolls-Royce University Technology Center, Virginia Polytechnic Institute and State University, 3046 Torgersen Hall, 620 Drillfield Drive, Blacksburg, VA 24061, USA

E-mail: shangs@vt.edu and rbatra@vt.edu

Received 17 March 2014, revised 27 June 2014
Accepted for publication 4 August 2014
Published 5 September 2014

Abstract

Due to complex interactions among the plasma jet, the coating powder particles and the carrier gas orthogonally injected into the plasma, the numerical simulation of a plasma thermal spray coating process is very challenging. In this paper, we numerically solve the system of nonlinear and coupled partial differential equations expressing the conservation of mass of species, the total mass, linear momentum and energy, as well as the k–ε turbulence model under pertinent initial and boundary conditions. The particle–plasma interaction is described by a drag force acting on particles and an equal and opposite force acting on the plasma. The lumped capacitance method is employed to model the particle heating and melting. Chemical reactions among species are considered. Whereas governing equations are written in the Eulerian description of motion, trajectories of powder particles are tracked using their Lagrangian description of motion. The mathematical model of the plasma process is validated by comparing computed results for the plasma, the particle temperature and the particle velocity with the corresponding test results taken from the literature. Significant contributions of the work include modelling effects of the carrier gas and the turbulence modulation introduced by particles which have not been considered in most previous two-dimensional and many three-dimensional studies. It is found that the consideration of turbulence modulation reduces the turbulent kinetic energy and its dissipation rate by more than 30% and 40%, respectively, in regions where particles are concentrated.

Keywords: plasma spray, plasma–particle interaction, turbulence modulation, particle injection, three-dimensional flow

(Some figures may appear in colour only in the online journal)

1. Introduction

Over the last two decades plasma thermal spray process that belongs to a large family of thermal spray processes has become a well-established and widely used technology in various industrial sectors such as aero gas turbine, automotive engines, oil and mining. Variants of the plasma spray process include atmospheric plasma spray (APS), vacuum or low-pressure plasma spray (VPS, LPPS), inert plasma spray (IPS), shrouded plasma spray (SPS) and controlled atmosphere plasma spray (CAPS) [1, 2]. Here we study the direct current (dc) APS schematically shown in figure 1.

As shown in figure 1, a mixture of gases (usually Ar, H_2, He and N_2) is heated to plasma temperature and is ionized by a high-intensity arc between the tip of the cathode and the water-cooled anode nozzle. Consequently, a plasma jet or plasma flame [3] emanates from the nozzle exit. The coating

[4] Author to whom any correspondence should be addressed.

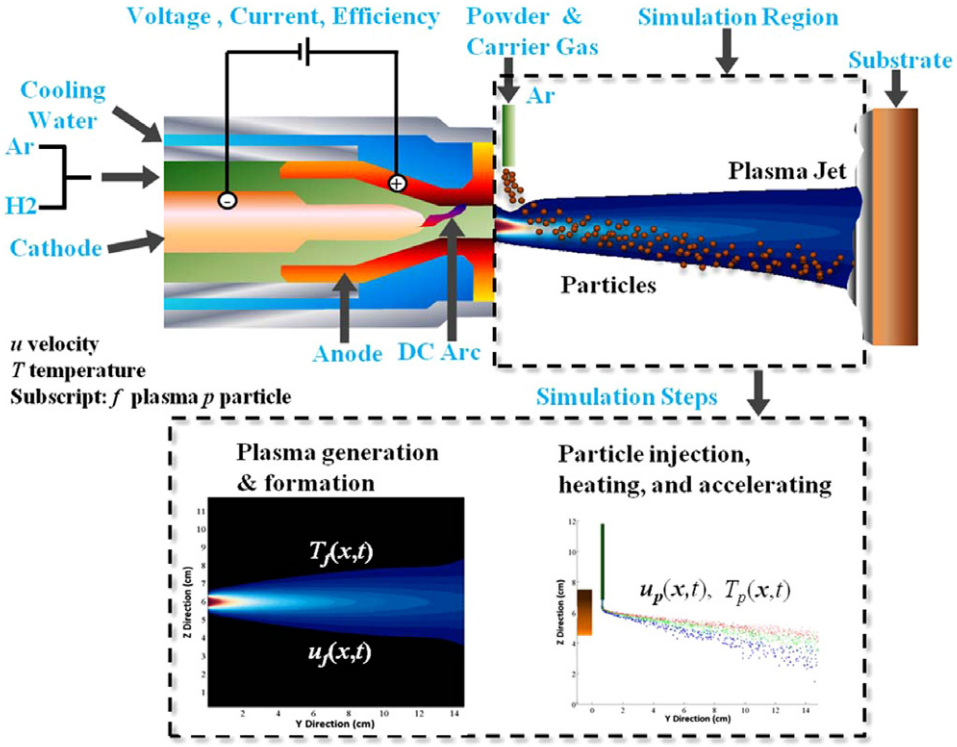

Figure 1. Schematics of a typical dc thermal plasma spray process (top) and its split into two parts (bottom). Here $\boldsymbol{u}$ = velocity, T = temperature and subscripts f and p stand for plasma flow and particle, respectively.

powder and the carrier gas are injected into the plasma through a powder port generally oriented perpendicular to the plasma jet axis. Through interactions with the plasma jet, the particles are accelerated, heated and partially melted before they strike the substrate and are deposited on it to form a coating.

A typical simulation of the plasma spray process can be divided into two parts: (1) plasma generation and formation, and (2) particle injection, heating and acceleration. Techniques for simulating the generation of the electric arc, arc fluctuations and plasma flow inside a dc torch are given in [4–12]. We note that three studies [13–15] predict the temperature and flow fields both inside and outside of a dc arc plasma torch. These authors have reported that the local anode arc-root attachment on the anode inner surface resulted in non-axisymmetric distribution about the nozzle axis of the plasma temperature and velocity at the circular cylindrical exit of the plasma torch. Here we simulate one case which considers this non-axisymmetric distribution of temperature and velocity of the plasma flow. However, due to the complexity of the plasma dynamics inside the torch, we follow many other published works and do not model the complex electromechanical interactions occurring within the gun. Plasma jet formation is simulated by solving the conservation equations of mass for each species, the total mass, linear momentum and energy along with transport equations representing the turbulence model [16–20]. Many phenomena such as chemical reactions, species mass diffusion, and heat transfer due to radiation and convection are included in the mathematical model. After injection into the hot and high-speed plasma jet, the coating powder is heated and accelerated. Effects of viscous drag force, particle rotation, thermophoresis, non-continuum effects, basset history term and turbulent dispersion exerted on the motion of a particle are summarized in [21]. However, only the drag force has been considered as the main driving force in most studies including this one. Various sources of heat exchange between the powder particles and the plasma are reviewed in [22], and are incorporated in the present mathematical model. A comprehensive review of particle heating, melting, re-solidification, and evaporation with consideration of the moving interface between the solid and the melted phases is given in [23]. Here we have employed the lumped heat capacitance model to simulate the particle heating because the Biot number in our numerical studies is expected to vary between 0.0017 and 0.3373. For particles going through the plasma where the convective heat transfer coefficient is very high, the particle surface temperature calculated by the lumped heat capacitance model may have a relatively larger error. The neglect of particle vaporization in our work could noticeably affect results for small particles since they have a high surface temperature. However, the short residual time in the plasma of these particles, 1–2 ms, due to their high axial velocities should reduce errors introduced by neglecting vaporization.

Despite the aforementioned simplifications, the complex coupling among the plasma jet, the carrier gas and the powder particles makes the theoretical modelling and numerical simulation of a dc APS process a challenging problem. Most earlier mathematical models are built for general three-dimensional (3D) deformations but the governing equations are solved by assuming the plasma flow to be axisymmetric

Table 1. Capabilities and shortcomings of several commonly used 3D simulation codes[a].

Ref.	CF	UF	CR	MCF	TWI	CG	TM	IHC
[32]	×			×		×		×
[13, 33, 36]						×		×
[37]	×			×		×		ESTET
[35, 38]					×		×	×
[39]	×	×	×	×	×	×		×
[40]	×	×		×	×			ANSYS Fluent
[41]	×	×		×	×	×		ANSYS Fluent
[42]		×	×					×
LAVA-P [28] (2D)	×	×	×	×				×
LAVA-3DI (present)	×	×	×	×	×	×	×	×

[a] CF stands for compressible flow, UF for unsteady flow, CR for chemical reaction, MCF for multi-component flow, TWI for two-way interaction, CG for carrier gas, TM for turbulence modulation, IHC for either the in-house code or the commercial code listed, × for the effect modelled.

(i.e. 2D) even when powder particles are injected in a direction perpendicular to the axis of the plasma flow, e.g. see [19, 20, 23–29]. Deformations studied in [23, 24, 27, 28] can be classified as pseudo-3D because they account for dispersions of the plasma induced by turbulent effects due to particle injection and predict 3D particle trajectories by considering plasma flow to be axisymmetric. However, the axisymmetric assumption is not valid unless the carrier gas and the powder particles are simultaneously injected all around the circumference of the plasma jet [13] which is generally not the case. The errors in the computed particle trajectories and temperatures introduced by this assumption have not been quantified yet.

In the last decade, simulation codes have been developed to find more realistic 3D temperature and velocity fields in the plasma jet [16–18, 30] and improved in-flight particle characteristics [13, 31–42]. Capabilities and shortcomings of several commonly used simulation codes are summarized in table 1. We note that the software LAVA, originally developed at the Idaho National Engineering and Environmental Laboratory (INEEL), can be used to analyse 2D axisymmetric temperature and velocity fields in the plasma jet, which is modelled as an unsteady, compressible, Newtonian, turbulent and chemically reacting ideal multi-component fluid mixture with temperature-dependent thermodynamic and transport properties [19, 20]. Wan *et al* [23, 28] developed LAVA-P, which is a pseudo-3D code to predict the particle temperature and velocity. However, it does not consider turbulence modulation that refers to the modification of the gas-phase turbulence due to the presence of particles. Although turbulence modulation has been extensively studied in particle-laden or multi-phase turbulent flows [43–54], only a few investigators [35, 38] have considered it in an ac APS, and that too by injecting only ten computational particles into the plasma flow. However, ten particles are too few due to the stochastic characteristics of turbulence and particle injection. Although the model used in [43–54] is 3D, the plasma is modelled as steady-state incompressible single-phase flow. Moreover, chemical reactions among species and effects of the carrier gas injection are neglected. Recently, Xiong *et al* [39] developed LAVA-P-3D by extending LAVA-P to include effects of the carrier gas and entrained particles on the plasma jet. However, they did not study effects of turbulence modulation on both plasma and particles.

In order to realistically consider complex interactions among plasma, particles and the carrier gas, and account for turbulence modulation we have generalized LAVA-P and call the modified software LAVA-3DI (3DI for three-dimensional interactions among the carrier gas, powder particles and the plasma) to better predict the plasma temperature and velocity, as well as the particle temperature, velocity, and 3D trajectories of the powder particles. The so-called 'standard approach' of turbulence modulation has been implemented in LAVA-3DI, and effects of the carrier gas and the turbulence modulation on the velocity, temperature and trajectories of particles have been examined in detail. In results presented herein, 21 969 particles are injected during the simulation of the thermal spray process, and at any time up to 2854 particles are present in the computational domain.

The rest of the paper is organized as follows. Various assumptions made to develop a mathematical model of the dc APS and the governing equations are summarized in section 2. Section 3 presents modelling of the motion and the heating of in-flight particles as well as the carrier gas injection. The turbulence modulation is introduced in section 4. Numerically computed plasma flow and particle characteristics using LAVA-3DI are compared with the corresponding experimental results in section 5. Detailed discussions of the carrier gas and the turbulence modulation effects are presented in section 6. In section 7, conclusions from the current work are summarized.

2. Mathematical model of plasma jet

Assumptions made to simulate the dc APS are summarized below.

(1) Plasma jet is a 3D unsteady, compressible, Newtonian, turbulent and chemically reacting ideal multi-component fluid mixture with only temperature-dependent thermodynamic and transport properties.
(2) The arc voltage fluctuations caused by the arc fluctuations are not considered. The mean value of the arc voltage is adopted, therefore, the amplitude of the temperature and the axial velocity at the nozzle exit remain constants.

(3) Plasma is in local thermodynamic equilibrium (LTE) and optically thin.
(4) Chemical reactions among different species including ionization, dissociation and recombination are considered.
(5) The effects of gravity and buoyance on the plasma jet and particle trajectories are neglected.
(6) Turbulence modulation due to the transverse injection of the powder particles is considered.

One way to distinguish between compressible and incompressible flow in gases is to find the Mach number (speed of the flow/local speed of sound). For the Mach number greater than about 0.3, significant compressibility effects may occur. Fauchais [55] has emphasized that most plasma flow models assume the flow to be incompressible even though the Mach numbers of the flow can be significantly more than 0.3. For the problems studied here, the Mach number in many computational cells exceeds 0.3 at $t = 3.5$ ms when the flow reaches the steady state without particle injection. Accordingly, we have modelled the flow as compressible.

We use rectangular Cartesian coordinate axes to describe 3D motion of the plasma and the injected particles. The conservation laws of the mass of each species, the total mass, the total linear momentum and the total energy of the thermal plasma are listed below as equations (1)–(4):

$$\frac{\partial \rho_i}{\partial t} + \nabla \cdot (\rho_i \boldsymbol{u}_f) = -\nabla \cdot \boldsymbol{J}_i + \dot{\rho}_i^{\mathrm{c}} + S_i^{\mathrm{cg}} \tag{1}$$

$$\frac{\partial \rho}{\partial t} + \nabla \cdot (\rho \boldsymbol{u}_f) = 0 \tag{2}$$

$$\frac{\partial \left(\rho \boldsymbol{u}_f\right)}{\partial t} + \nabla \cdot (\rho \boldsymbol{u}_f \otimes \boldsymbol{u}_f) = -\nabla \left(p + \frac{2}{3}\rho k\right) + \nabla \cdot \sigma + \boldsymbol{S}_{pm} + \boldsymbol{S}_{\mathrm{cgm}} \tag{3}$$

$$\frac{\partial (\rho e)}{\partial t} + \nabla \cdot (\rho e \boldsymbol{u}_f) = -p \nabla \cdot \sigma - \nabla \cdot \boldsymbol{q} + \rho \varepsilon + \dot{Q}_{\mathrm{c}} - \dot{Q}_{\mathrm{R}} + S_{pe} + S_{\mathrm{cge}}. \tag{4}$$

Here ρ_i is the mass density of the species i, t is the time, $\boldsymbol{u}_f$ is the mean plasma velocity, ρ is the mass density of plasma, $\boldsymbol{J}_i$ is the diffusional mass flux of species i, $\dot{\rho}_i^{\mathrm{c}}$ is the rate of change of ρ_i due to chemical reactions, ρ is the total mass density of the plasma, p is the pressure, σ is the viscous stress tensor, k is the turbulent kinetic energy, ε is the viscous dissipation rate per unit mass, $\boldsymbol{S}_{pm}$ is the momentum source/sink term introduced by injected particles described in the next section, e is the total thermal specific internal energy, $\boldsymbol{q}$ is the heat flux vector, S_{pe} is the energy source/sink term introduced by injected particles, $\dot{Q}_{\mathrm{c}}$ is the rate of change of ρe due to chemical reactions [20] and $\dot{Q}_{\mathrm{R}}$ is the radiative heat loss, which is modelled as a simple temperature-dependent volumetric sink term [56]. Quantities S_i^{cg}, $\boldsymbol{S}_{\mathrm{cgm}}$ and S_{cge} are the mass, the momentum and the energy source term introduced by the carrier gas, which will be explained below.

The viscosity and the thermal conductivity of the mixture are obtained using the rule of mixtures from the mole fractions of the species and the temperature-dependent viscosity and thermal conductivities of the species. These values at a given temperature are interpolated from the tabulated property values of argon, hydrogen and air at different temperatures. The reaction contribution to the thermal conductivity is not included, as it is an indirect effect of species diffusion which is automatically accounted for in the model as shown in equation (1). Ionization, dissociation and recombination of species Ar, Ar^+, H_2, H, H^+, N_2, N_2^+, N, O_2, O, O^+, e^-, OH and H_2O are considered. The set of chemical reactions is listed in appendix B. Details of these chemical reactions are given in [57]. Whereas the gravity force will bend the plasma jet downwards, the buoyancy force will bend it upwards. We note that the mass density of the plasma mixture is less than that of the air, hence the effect of the gravity force on the plasma can be neglected as compared with that of the inertia force. The effect of the buoyancy on the plasma flow is considered in [58, 59], where it is concluded that the plasma jet is nearly axisymmetric since the buoyancy force is negligible as compared with the inertia force [58]. Similarly, the gravity and the buoyancy forces will have negligible effects on particle trajectories as compared with that of the viscous drag force.

Even though there are many Reynolds averaged Navier–Stokes equations (RANS)-based turbulence models such as the standard k–ε and its extensions, none of them is general enough to be applicable to every case. Out of these models, the k–ε model is easy to implement, computationally inexpensive, relatively robust, and provides useful semi-quantitative results of acceptable accuracy. Therefore, the standard k–ε model described by transport equations (5) and (6) is used in this work to simulate turbulence.

$$\frac{\partial \rho k}{\partial t} + \nabla \cdot (\rho k \boldsymbol{u}_f) = -\frac{2}{3}\rho k \nabla \cdot \boldsymbol{u}_f + \nabla \cdot [(\mu + \mu_t)\nabla k] + \phi - \rho\varepsilon + S_{pk} \tag{5}$$

$$\frac{\partial \rho \varepsilon}{\partial t} + \nabla \cdot (\rho \varepsilon \boldsymbol{u}_f) = \left(c_3 - \frac{2}{3}c_1\right)\rho\varepsilon \nabla \cdot \boldsymbol{u}_f + \nabla \cdot \left[\left(\mu + \frac{\mu_t}{\sigma_\varepsilon}\right)\nabla\varepsilon\right] + \frac{\varepsilon}{k}(c_1\phi - c_2\rho\varepsilon) + S_{p\varepsilon}. \tag{6}$$

In these equations μ is the viscosity, c_1, c_2, c_3 and σ_ε are the model coefficients which equal 1.44, 1.92, −1.0 and 1.3, respectively, and ϕ is the turbulence production due to viscosity. The turbulent viscosity μ_t is defined as $\mu_t = \mathrm{c}_\mu \rho k^2/\varepsilon$ in which $c_\mu = 0.09$. Quantities S_{pk} and $S_{p\varepsilon}$ are the source/sink terms due to turbulence modulation caused by the particle–turbulence interaction. Expressions for S_{pk} and $S_{p\varepsilon}$ are given in section 4. Supplementary equations to close the system of equations (i.e. to have the number of unknowns equal to the number of equations) are listed in appendix A.

We use the finite-difference computational algorithm for the temporal and the spatial differencing scheme given in [20] to numerically solve the system of equations under prescribed initial and boundary conditions (BCs). The temporal differencing scheme is a first-order conditionally stable explicit method. The spatial difference approximations are derived by the control volume or the finite-volume approach. All terms other than convection are evaluated as simple centred differences. Convection terms are evaluated by a weighted average of centred and upwind differencing, with the option of automatic local computations of the weighting

factor. The time step for computing a stable solution is given by equation (47) of [20]. Typically, it is less than the time taken for a wave to travel across the smallest cell in the mesh. The order of accuracy of the spatial scheme is not given in [20] but is anticipated to be 1.

3. Modelling of particle injection

The computation of powder particles' velocities, temperatures and trajectories are based on the following assumptions:

(1) The viscous drag force acting on a particle is the only driving force. The force by the thermal gradient can be of the same order of magnitude as the gravitational acceleration, but here both are not considered relative to the drag force which is three or four orders of magnitude higher [60].
(2) Particles are spherical.
(3) The lumped capacitance method is adequate to compute heating and melting of particles.
(4) There is no evaporation of any portion of particles.

3.1. Equation of motion for a particle

Particle's motion is governed by Newton's second law of motion. Thus, the acceleration of a particle equals the drag force divided by its mass,

$$\frac{\mathrm{d}\boldsymbol{u}_p}{\mathrm{d}t} = \frac{3}{8}\frac{\rho}{\rho_p}\frac{C_\mathrm{D}}{r_p}\left|\boldsymbol{u}_\mathrm{rel}\right|\boldsymbol{u}_\mathrm{rel} \tag{7}$$

$$\boldsymbol{u}_\mathrm{rel} = \boldsymbol{u}_f + \boldsymbol{u}' - \boldsymbol{u}_p. \tag{8}$$

Here ρ_p is the particle mass density, r_p is the particle radius, u_p is the particle velocity, u_rel is the velocity of the particle relative to that of the plasma, $\boldsymbol{u}'$ is the turbulence dispersion and is a random variable, and C_D is the drag coefficient. The expression for the drag force coefficient C_D, taken from [21], is

$$C_\mathrm{D} = \left(\frac{24}{Re_p} + \frac{6}{1+\sqrt{Re_p}} + 0.4\right) f_\mathrm{prop}^{-0.45} f_\mathrm{Kn}^{0.45} \tag{9}$$

$$Re_p = \frac{\rho_p D_p \left|\boldsymbol{u}_\mathrm{rel}\right|}{\mu} \tag{10}$$

where Re_p is the Reynolds number of the particle, μ is the plasma viscosity, D_p is the diameter of the particle, $f_\mathrm{prop}^{-0.45}$ is a correction factor for strongly varying plasma properties, and $f_\mathrm{Kn}^{0.45}$ is a correction factor that incorporates non-continuum effects. Expressions for $f_\mathrm{prop}^{-0.45}$ and $f_\mathrm{Kn}^{0.45}$ are

$$f_\mathrm{prop}^{-0.45} = \left(\rho_\infty \mu_\infty / \rho_\mathrm{w} \mu_\mathrm{w}\right)^{-0.45} \tag{11}$$

$$f_\mathrm{Kn}^{0.45} = \frac{1}{\left[1 + \left(\frac{2-a}{a}\right)\left(\frac{\gamma}{1+\gamma}\right)\frac{4}{Pr_\mathrm{w}}Kn\right]^{0.45}}. \tag{12}$$

Here ρ_∞ and μ_∞ (ρ_w and μ_w) are, respectively, the mass density and the viscosity of the plasma corresponding to the free-stream (the wall) temperature, a is the thermal accommodation coefficient, γ is the ratio of specific heats, Pr_w is the Prandtl number of the plasma at the surface temperature of the particle and K_n is the Knudsen number based on an effective mean free path length. In equation (8), the velocity fluctuation $\boldsymbol{u}'$ represents the turbulence dispersion and is a random variable. Each component of $\boldsymbol{u}'$ is distributed according to a Gaussian distribution, e.g. see [61]. It follows from equations (7), (9) and (10) that the acceleration of a particle is inversely proportional to its volume.

The momentum source/sink term, $\boldsymbol{S}_{pm}$, introduced by the particle loading is given by

$$\boldsymbol{S}_{pm} = \sum_{k=1}^{\mathrm{NP}} \frac{3}{8}\frac{\alpha_k \rho C_\mathrm{D}^k}{r_p^k}\left|\boldsymbol{u}_\mathrm{vel}^k\right|\boldsymbol{u}_\mathrm{vel}^k. \tag{13}$$

Here the superscript k indicates the kth particle, NP equals the total number of computational particles, and the particle volume fraction α_k is given by

$$\alpha_k = \frac{4}{3}\pi\left(r_p^k\right)^3 / V_\mathrm{cell}^k \tag{14}$$

where r_p^k is the radius of the kth particle, and V_cell^k is the volume of the cell containing the kth particle. The source term, $\boldsymbol{S}_{pm}$, is non-zero only in those computational cells that have the centre of a powder particle.

3.2. Particle energy transport

Using the lumped capacitance method, the particle heating and melting is governed by

$$V_p \rho_p C_p \frac{\partial T_p}{\partial t} = A_\mathrm{s} h (T_f - T_p) \qquad \text{for } T_p \neq T_m \tag{15}$$

$$V_p \rho_p L_m \frac{\partial \chi_p}{\partial t} = A_\mathrm{s} h (T_f - T_p) \qquad \text{for } T_p = T_m \tag{16}$$

where V_p is the volume of the particle, T_f is the temperature of the plasma, T_p is the particle temperature, C_p is the heat capacity, A_s is the surface area of the particle, L_m is the latent heat of fusion, h is the heat transfer coefficient and χ_p is the melt fraction of the particle.

The internal energy source/sink term, S_{pe}, appearing in equation (4), due to heat conduction and exchange of kinetic energy between the plasma jet and the particles is given by

$$S_{pe} = \sum_{k=1}^{\mathrm{NP}} \alpha_k \left[h(T_p^k - T_f) + \frac{3}{8}\frac{\rho C_\mathrm{D}^k}{r_p^k}\left|\boldsymbol{u}_\mathrm{vel}^k\right|^3\right]. \tag{17}$$

3.3. Carrier gas injection

The carrier gas injected with the powder particles provides a sufficiently high velocity to the particles so that they penetrate into the fast moving and high-temperature plasma field [41]. The carrier gas is modelled as source/sink terms S_i^cg, $\boldsymbol{S}_\mathrm{cgm}$ and S_cge included, respectively, in the conservation equations of mass, momentum and energy in the plasma of the cells into

which the carrier gas and the powder particles are injected:

$$S_i^{\mathrm{cg}} = \dot{m}_i^{\mathrm{cg}} / V_{\mathrm{tl}} \tag{18}$$

$$\boldsymbol{S}_{\mathrm{cgm}} = \frac{1}{2}\dot{m}^{\mathrm{cg}} v_{\mathrm{inj}} \boldsymbol{\theta} / V_{\mathrm{tl}} \tag{19}$$

$$\begin{aligned} S_{\mathrm{cge}} &= \frac{1}{V_{\mathrm{tl}}} \sum_{i=1}^{\mathrm{NSP}} \dot{m}_i^{\mathrm{cg}} e(T_f) \\ &= \frac{1}{V_{\mathrm{tl}}} \sum_{i=1}^{\mathrm{NSP}} \dot{m}_i^{\mathrm{cg}} \left[\frac{1}{M_i} \left((h_i(T_f) - h_i^{\mathrm{ref}}) - R_{\mathrm{g}} T_f \right) \right]. \end{aligned} \tag{20}$$

Here the subscript i denotes the ith species, $\dot{m}_i^{\mathrm{cg}}$ is the carrier gas mass flow rate, V_{tl} is the sum of the volume of cells that contain the powder port exit, $\dot{m}^{\mathrm{cg}}$ is the total carrier gas mass flow rate, v_{inj} is the injection velocity of the carrier gas, $\boldsymbol{\theta}$ is the unit vector along the direction of the carrier gas injection, NSP is the total number of species, M_i is the molecular weight, h_i is the enthalpy taken from the JANAF thermochemical table that gives h_i as a function of temperature, h_i^{ref} is the reference enthalpy at 0 K and R_{g} is the universal gas constant.

The powder port is not modelled in this work. If the circular exit area of the powder port overlaps more than one computational cell, then the source/sink term is divided among these cells based on the area overlapped of each cell. The temperature and the pressure of the carrier gas equal those of the ambient air.

3.4. Boundary and initial conditions

A virtual layer is assumed to exist around the boundary of the computational domain for applying BCs. We recall that the plasma generation inside the torch has not been simulated. Accordingly, we assume that profiles of the temperature, the velocity and the turbulence variables at the nozzle exit are given by equation (21), and note that the assumed plasma flow and the temperature profile at the nozzle exit are axisymmetric with respect to the torch axis. The effects of non-symmetric BCs at the nozzle exit on the plasma flow and the particles' trajectories and temperatures are studied in section 5.3. Even when the BCs at the nozzle exit are axisymmetric, upon injection of the powder particles and the carrier gas the axisymmetry of the flow is lost. Accordingly, we still simulate the 3D flow.

$$\begin{cases} T_f(X,Z) = (T_0 - T_{\mathrm{w}i}) \left[1 - \left(\dfrac{r}{R_i} \right)^{n_T} \right] + T_{\mathrm{w}i} \\ u_f^Y(X,Z) = V_0 \left[1 - \left(\dfrac{r}{R_0} \right)^{n_V} \right] \\ u_f^X(X,Z) = u_f^Z(X,Z) = 0 \\ k(X,Z) = \kappa V_0 \left[\dfrac{\partial u_f^Y}{\partial r} \Big/ \left(\dfrac{\partial u_f^Y}{\partial r} \right)_{\max} \right] \\ \varepsilon(X,Z) = k(X,Z)^{3/2} / (0.0075\, \delta_{0.1} / c_\mu^{3/4}) \end{cases} \left(\begin{array}{l} \text{on plane} \\ Y = 0,\ r = \sqrt{(X - X_0)^2 + (Z - Z_0)^2} \leqslant R_i \end{array} \right). \tag{21}$$

Here (X_0, Z_0) is the nozzle exit centre, T_0 and V_0 are, respectively, amplitudes of the temperature and the axial velocity profiles, and the coefficients n_T and n_V determine how fast the temperature and the axial velocity decay in the radial direction. Values of T_0, V_0, n_T and n_V are selected to match, as closely as possible, the known input gas flow rates and the torch power. This is accomplished by equating these quantities to those obtained by integrating the resulting mass and the energy over the nozzle exit area. Thus, their values depend on the operating conditions and the torch nozzle diameter, and are determined using an iterative approach till the difference between the input and the output mass flow rate and the power is less than 1%.

We now describe three techniques used in previous works to determine values of T_0, V_0, n_T and n_V. In [29], values of the four variables are found by curve fitting the experimental temperature and velocity radial profiles measured close enough to the torch front face using equation (21). In [28], instead of the radial profile, only T_0 and V_0 are measured, and values of n_T and n_V are found by matching the total mass and the energy flow rate out of the torch nozzle with that input into the torch. In the absence of test data, one can assume values of either n_T and n_V [62] or T_0 and V_0 and determine values of the other two parameters based on the balance of energy and the mass flow rate, as was done in [28]. In this paper, we assumed n_T and n_V and iteratively found T_0 and V_0 so that the input mass rate and the input power differed by less than1% of their values at the nozzle exit. The BCs for the turbulence parameter $k(X, Z)$ listed in equation (21) are the same as that used in [29], $(\partial u_f^Y/\partial r)_{\max}$ is the largest value of the axial velocity gradient in the radial direction at the torch exit, the parameter κ determines the shape of the profile, and $\delta_{0.1}$ equals the jet width at the location where $u_f^Y = 0.1 V_0$.

The torch wall is treated as a solid boundary where no-slip condition holds. For $R_{\mathrm{i}} < r < R_{\mathrm{o}}$ and $Y = 0$, BCs on the torch wall are given by equation (22). That is, the temperature varies logarithmically from $T_{\mathrm{w}i}$ at $r = R_{\mathrm{i}}$ to T_∞ at $r = R_{\mathrm{o}}$. T_∞ is usually taken as the ambient temperature.

$$\begin{cases} T_f(X,Z) = T_{\mathrm{w}i} + (T_\infty - T_{\mathrm{w}i}) \dfrac{\ln(r/R_{\mathrm{i}})}{\ln(R_{\mathrm{i}}/R_{\mathrm{o}})} \\ u_f^X(X,Z) = u_f^Y(X,Z) = u_f^Z(X,Z) = 0 \\ k(X,Z) = 0 \\ \varepsilon(X,Z) = 0 \end{cases} \left(\text{on plane } Y = 0,\ R_{\mathrm{i}} \leqslant \sqrt{(X - X_0)^2 + (Z - Z_0)^2} \leqslant R_{\mathrm{o}} \right). \tag{22}$$

On lateral surfaces of the computational domain, depicted in figure 2, BCs given by either equation (23) or by equation (24) are applied. For $\boldsymbol{u}_f \cdot \boldsymbol{n} > 0$, equation (23) holds, i.e. boundaries are thermally insulated and gradients of $\boldsymbol{u}_f$,k and ε are tangent to the boundary. Otherwise, the temperature is set equal to the ambient temperature, and $k = \varepsilon = 0$.

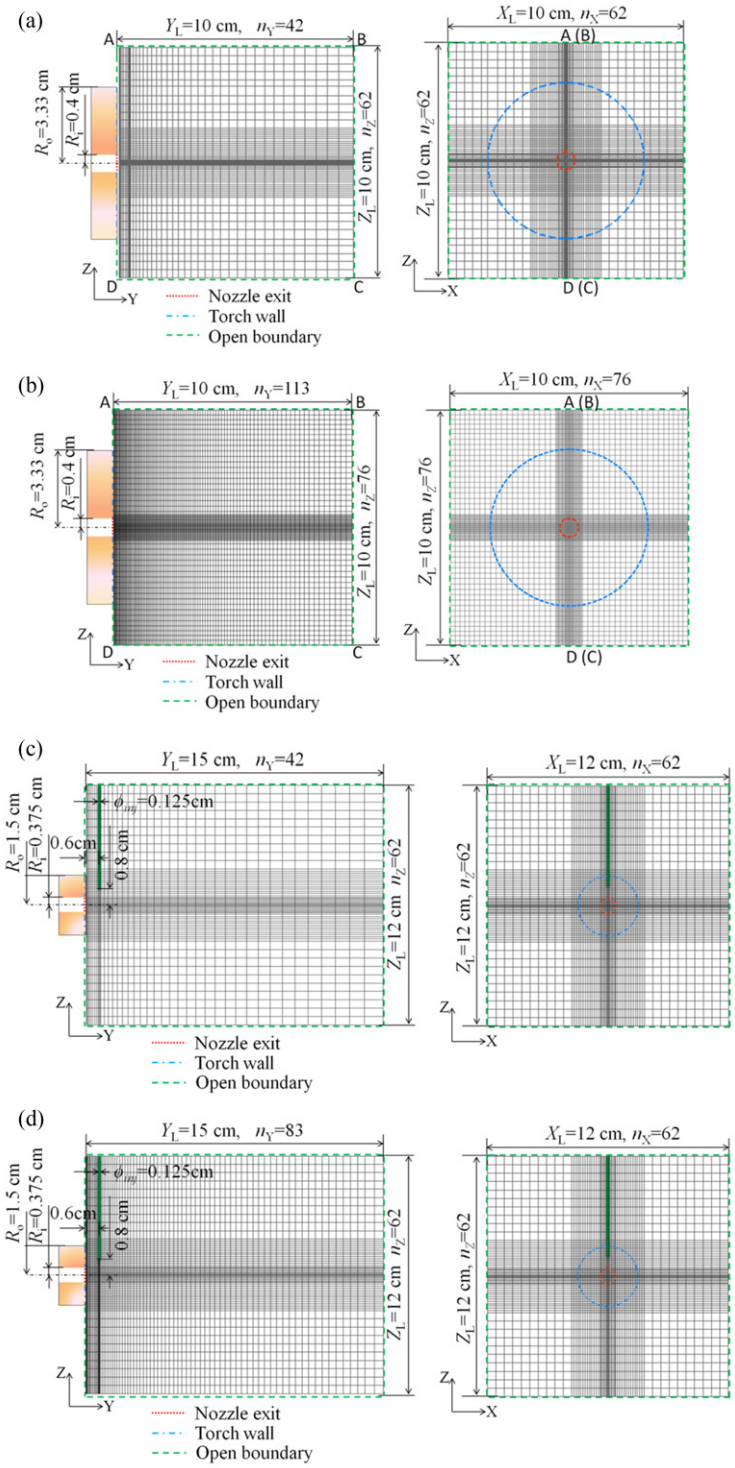

Figure 2. Nozzle geometry, computational mesh and BCs applied in (*a*) case 1 with a coarse mesh, (*b*) case 1 with a fine mesh, (*c*) case 2 with a coarse mesh and (*d*) case 2 with a fine mesh.

Outward flow:

$$\begin{cases} \partial T_f(X,\ Y,\ Z)/\partial n = 0 \\ \partial \boldsymbol{u}_f(X,\ Y,\ Z)/\partial n = 0 \\ \partial k(X,\ Y,\ Z)/\partial n = 0 \\ \partial \varepsilon(X,\ Y,\ Z)/\partial n = 0 \end{cases} \left(\begin{array}{l} \text{on planes } X = 0;\ X = X_L;\ Z = 0;\ Z = Z_L; \\ Y = 0,\ \sqrt{(X - X_0)^2 + (Z - Z_0)^2} \geqslant R_0;\ Y = Y_L \end{array} \right). \tag{23}$$

Inward flow:

$$\begin{cases} T_f(X,\ Y,\ Z) = T_{\text{abm}} \\ \partial \boldsymbol{u}_f(X,\ Y,\ Z)/\partial n = 0 \\ k(X,\ Y,\ Z) = 0 \\ \varepsilon(X,\ Y,\ Z) = 0 \end{cases} \left(\begin{array}{l} \text{on planes } X = 0;\ X = X_L;\ Z = 0;\ Z = Z_L; \\ Y = 0,\ \sqrt{(X - X_0)^2 + (Z - Z_0)^2} \geqslant R_0;\ Y = Y_L \end{array} \right). \tag{24}$$

Initially, the computational domain is filled with quiescent air at ambient temperature. Thus

$$\begin{cases} T_f(X,\ Y,\ Z,\ t=0) = T_{\text{abm}} \\ \boldsymbol{u}_f(X,\ Y,\ Z,\ t=0) = 0 \\ k(X,\ Y,\ Z,\ t=0) = 0 \\ \varepsilon(X,\ Y,\ Z,\ t=0) = 0. \end{cases} \tag{25}$$

4. Turbulence modulation

The effect of injected powder particles on the turbulence kinetic energy and the energy dissipation is significant, and should be considered when the volume fraction α_p of particles is between 10^{-6} and 10^{-3}, e.g. see [46, 63]. Furthermore, for $\alpha_p > 10^{-3}$, collisions among particles should be considered. We plan to consider collisions among powder particles in a future work.

Four mechanisms for turbulence modulation are: (i) transfer of energy through the drag force, (ii) particle interactions with turbulent eddies, (iii) turbulence production from wake formation and vortex shedding, and (iv) energy transfer arising from the crossing trajectory effect. Although turbulence modulation has been studied for a long time, there is no generally accepted model that is applicable for all flow conditions [49]. The turbulence modulation algorithms have been classified into two categories [50]: standard method [48] and consistent method [49]. The standard method considers the turbulent fluctuations as a sink, while the consistent method can predict both the turbulence augmentation and attenuation. In most cases, the transfer of energy through the drag force acts as a sink of turbulent kinetic energy and is studied using several turbulence modulation models [51]. A recently proposed standard approach [51] that accounts for the change in the fluid velocity correlation as a result of the crossing trajectory effect is adopted in this paper. In this model, the source/sink term, S_{pk}, in the turbulent kinetic energy equation (5) is given by

$$S_{pk} = 2k \sum_{k=1}^{\text{NP}} \left[\frac{\alpha_k}{\tau_p^k} \left(1 - \frac{\tau_k^*}{\tau_k^* + \tau_p^k} \right) \right] \tag{26}$$

$$\tau_p^k(C_{\text{D}}) = \frac{4}{3\mu} \frac{\rho_p (D_p^k)^2}{Re_p^k C_{\text{D}}^k} \tag{27}$$

$$\frac{1}{\tau_k^*} = \frac{1}{0.135k/\varepsilon} + \frac{|\boldsymbol{u}_{\text{rel}}|}{0.22k^{3/2}/\varepsilon} \tag{28}$$

where τ_p^k is the response time of the kth computational particle. The turbulent kinetic energy k in equation (26) should not be confused with the sub- and the superscript k. The source term $S_{p\varepsilon}$ in the ε-equation (6) is taken to be proportional to S_{pk}, i.e.

$$S_{p\varepsilon} = C_{\varepsilon 3} \frac{\varepsilon}{k} S_{pk}. \tag{29}$$

The suggested value of $C_{\varepsilon 3}$ in the standard method [64] is 1.1; however, this value is not universally accepted [65].

Table 2. Values of operating parameters.

Parameter	Case 1 (Miller SG-100 torch)	Case 2 (Sulzer Metco 9MB torch)
Current (A)	900	500
Voltage (V)	15.4	70
Power efficiency (%)	70	70
Ambient gas	Air	Air
Ambient gas temperature (K)	300	300
Ambient gas pressure (kPa)	85.5	85.5
Primary gas and flow rate (standard litre per minute, slm)	35.4 Ar	40 Ar
Secondary gas and flow rate (slm)	N/A	12 H_2
Carrier gas and flow rate (slm)	N/A	5 Ar
Carrier gas injection velocity ($m\,s^{-1}$)	N/A	67.93
Torch wall temperature (K)	700	700
Nozzle radius (mm)	4	3.75
Torch outer radius (mm)	33.3	15
Spray distance (cm)	10	15
Feed rate ($g\,min^{-1}$)	N/A	20

Table 3. Values of parameters in inlet BCs.

	Case 1	Case 2
T_0 (K)[a]	11 000	13 000
T_{wi} (K)	700	700
T_∞ (K)	300	300
n_T	2.3	6.0
V_0 ($m\,s^{-1}$)[a]	1100	3000
n_V	1.4	1.2
κ	0.000 15	0.015

[a] Initial input value of T_0 and V_0. Converged values of T_0 and V_0 output from LAVA-3DI equal 12 913 K and 1092 $m\,s^{-1}$, respectively, for case 1, and 13 092 K and 3056 $m\,s^{-1}$ for case 2.

5. Comparison of computed and experimental plasma jet formation and in-flight particle characteristics

5.1. Processing parameters, geometry, computational mesh and BCs

Two different commercial torches, Miller SG-100 (hereafter referred to as case 1) and Sulzer Metco 9MB (case 2), are considered. Since the plasma formation in the torch is not simulated, only dimensions of the torch at the exit of the plasma play a role in our work. Values of operating parameters adopted in this work and listed in table 2 and of those in the BCs

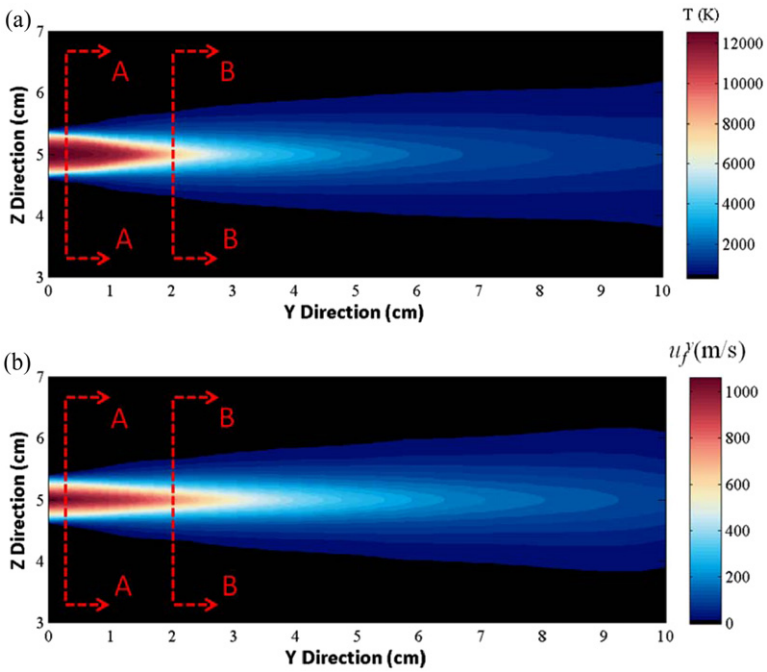

Figure 3. Contour plots of the computed (*a*) temperature, and (*b*) axial velocity, u_y, at the mid-plane ABCD, $X = 6$ cm. Cross-section AA is at $Y = 0.2$ cm and BB at $Y = 2$ cm. Temperature and velocity profiles on these cross-sections are plotted in figure 4.

in table 3 are the same as those used by other investigators. The carrier gas injection velocity equals the average velocity determined from the carrier gas flow rate $\dot{Q}_{\rm cg}$and the exit area $A_{\rm inj}$ of the injector [62]:

$$v_{\rm inj} = \frac{\dot{Q}_{\rm cg}}{A_{\rm inj}}. \tag{30}$$

The geometry of the simulation domain, its discretization into cells and BCs are exhibited in figure 2. For case 1, see figures 2(*a*) and (*b*), the size of the computational domain is $X_L = Y_L = Z_L = 10$ cm. The computational domain is divided into 161 448 (652 688) cells in the coarse (the fine) mesh with the number of cells in X, Y and Z directions given by $n_X = 62(76), n_Y = 42(113)$ and $n_Z = 62(76)$, respectively. For case 2, see figures 2(*c*) and (*d*), the size of the computational domain is $X_L = 12$ cm, $Y_L = 15$ cm and $Z_L = 12$ cm. We set $n_X = 62, n_Y = 42(83)$ and $n_Z = 62$, resulting in 161 448 (319 052) computational cells in the coarse (the fine) mesh. For both problems studied, the cell size is smaller near the torch outlet and the entrainment regions than that away from these regions. It enables one to better capture the large gradients in the solution variables that are likely to occur in these areas. Since we solved the 3D problems using rectangular Cartesian coordinates, rectangular cells are used to approximate a disc area of the nozzle exit. The maximum difference between the physical and the approximated areas is 1.6% in current studies. This difference can be further reduced by refining the mesh in the region of the nozzle exit. As mentioned in section 3.4, the iterative approach will tune T_0 and V_0 to match the torch power and mass flow rate to their values at the nozzle exit. Therefore, the difference in the simulated and actual areas of the nozzle exit should not have noticeable effect on the computed results. In order to delineate the effect of the size of the computational domain upon the solution, we compute results for three domain sizes for case 2, namely, 9.48 cm × 10.56 cm × 9.48 cm, 12 cm × 15 cm × 12 cm and 16.2 cm × 17.1 cm × 16.2 cm. The maximum differences in the temperature and the magnitudes of the velocity distributions on the central axis and the radial profiles at 0.25 cm and 1.96 cm away from the nozzle exit between the largest and the smallest computational domains are, respectively, 3.82% and 2.59%. Thus, the intermediate size computational domain listed above should give reasonably accurate results.

5.2. Plasma jet formation

For problem 1 we study the discharge into ambient air of pure argon (Ar) plasma formed within the torch. Results for the axial velocity and the temperature variation within a small region of the mid-plane ABCD, computed without powder particle injection and using the fine mesh, plotted in figure 3 are for $t = 4$ ms when the flow has reached steady state. The variations of the temperature and of the axial velocity on the centreline at $t = 4$ ms are compared in figures 4(*a*) and (*b*) with the corresponding experimental data taken from [29]. Without particle injection and the carrier gas flow, the plasma jet is axisymmetric. The decaying trends of the temperature and the axial velocity are well captured, and the computed results agree with the corresponding test values. Computed variations of the temperature and the axial velocity in the radial direction at two different axial locations, i.e. cross-sections AA and BB, are compared with the corresponding experimental values in figures 4(*c*)–(*f*). It is clear that the two sets of results agree well with each other. By comparing the two sets of results

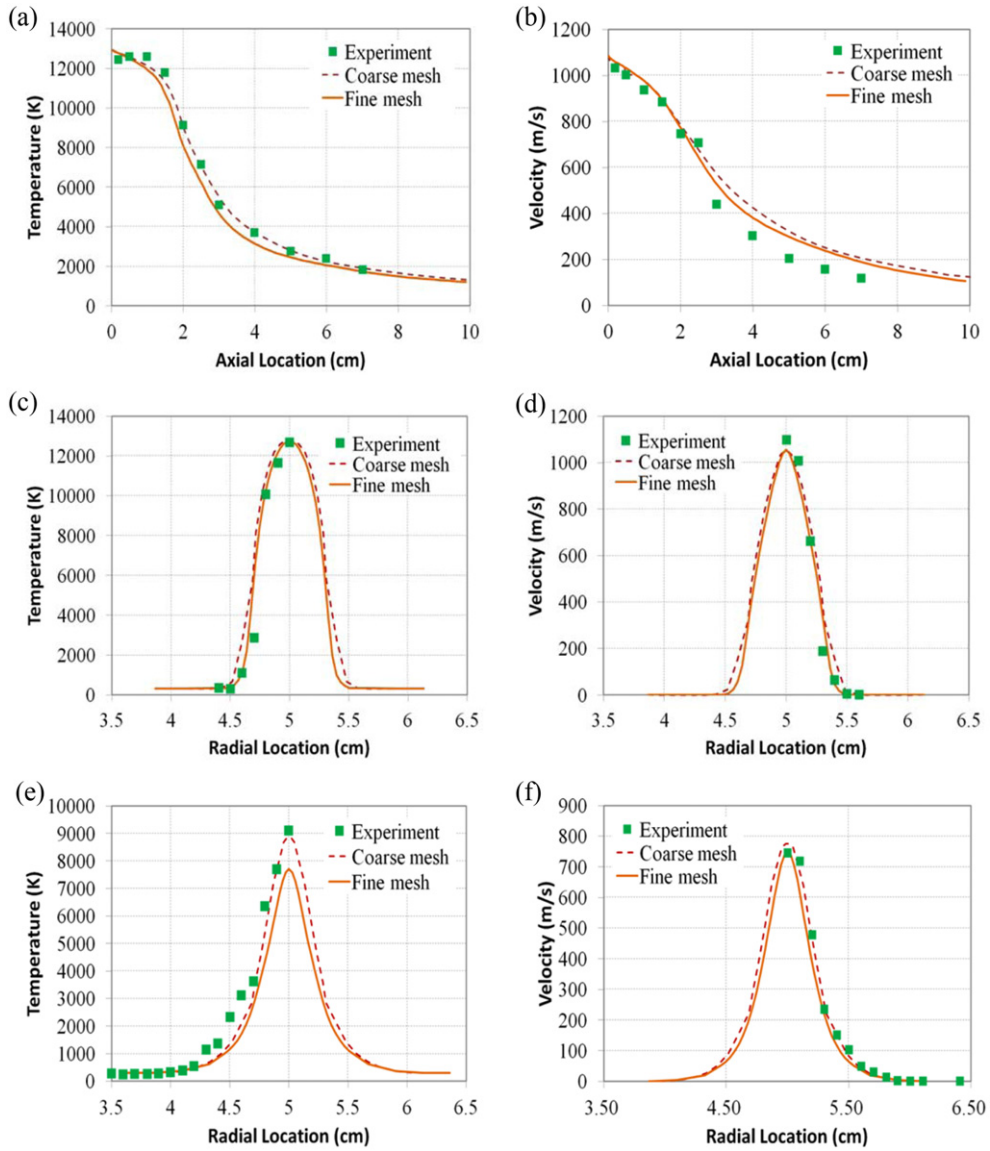

Figure 4. Comparison between the computed and the experimental results [29]: (*a*) centreline temperature, (*b*) centreline axial velocity u_y; (*c*) radial variation of the temperature on cross-section AA, (*d*) radial variation of the axial velocity u_y on cross-section AA, (*e*) radial variation of the temperature on cross-section BB and (*f*) radial variation of the axial velocity u_y on cross-section BB.

plotted in figure 4 one can conclude that both the coarse and the fine meshes give results close to each other.

5.3. Plasma flow with injection of particles

In problem 2 we simulate the injection of ZrO_2 particles into the plasma for the Sulzer Metco 9MB torch for values of operating parameters listed in table 2, of parameters appearing in BCs given in table 3, and those of ZrO_2 particles provided in table 4. The computed species distributions are plotted in figure 5 at $t = 3.5$ ms for the case of no particle injection, no arc fluctuation, and both axisymmetric and non-axisymmetric inlet BCs depicted in figure 6. For the particle diameter varying between 30 and 100 μm, probabilities of having particles of diameter in different ranges, taken from [23], are plotted in figure 8.

Table 4. Values of parameters for ZrO_2 particles.

	Value
Mass density, ρ_p (g cm^{-3})	5.89
Particle size range (μm)	30–100
Mean particle diameter, $D_{p\,\mathrm{mean}}$ (μm)	58
Injection velocity, v_{inj} (m s^{-1})	14.5
Melting temperature, T_{m} (K)	2950
Thermal conductivity, k_p (W m^{-1} K^{-1})	2.0
Heat capacity, C_p (J kg^{-1}K^{-1})	580

With time reckoned from the instant of turning on the torch and particles injected at $t = 6$ ms, the computed temperature and axial velocity distributions of the plasma on two different cross-sections away from the nozzle exit are shown in figure 7 at $t = 18$ ms. One can observe that the plasma flow is affected

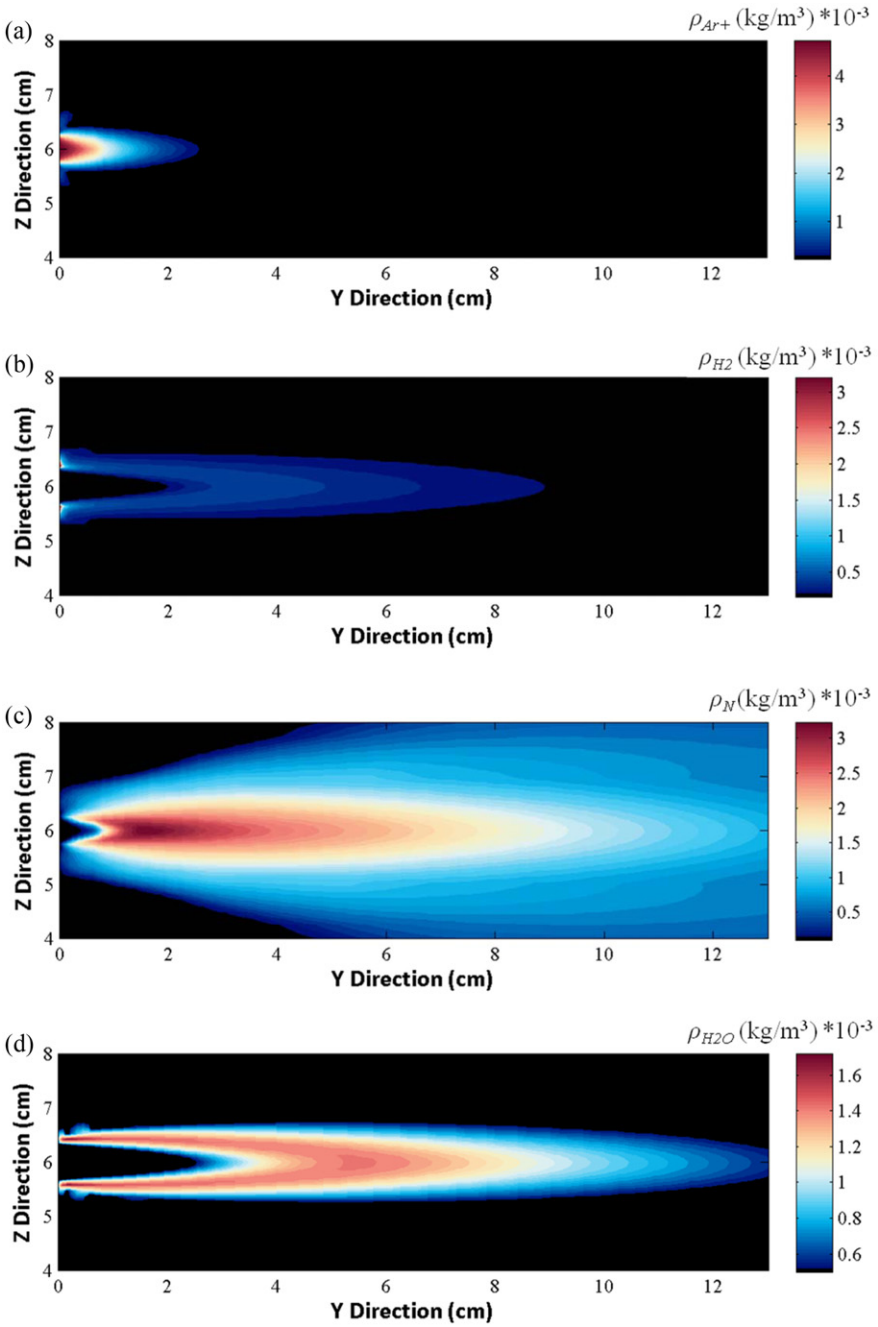

Figure 5. Species distributions of (*a*) Ar^+, (*b*) H_2, (*c*) N and (*d*) H_2O.

by the non-axisymmetric BCs. The computed temperature and the axial velocity of three groups of particles at $t = 18$ ms are exhibited in figure 9 for the axisymmetric BCs at the nozzle exit, and solid curves are least-squares fit to the computed values. It can be observed that the computed temperature and velocity of particles having diameters in the range 30–42 μm are closer to the test data of [66] than those of particles of other diameters. As mentioned in [66], the average particle trajectory patterns were obtained with a spray pattern trajectory (SPT) sensor and the average velocity of the particles was measured with a laser Doppler velocimetry system. Since the SPT sensor was focused on a very small region near the nozzle axis, velocities of small particles, which moved close to the axial axis, are captured. Therefore, the computed axial velocity of smaller particles is closer to those measured experimentally. The mean particle temperature is measured by IPP 2000, which measured the temperature of particles moving through the focused cross-section [23]. The computed particle surface temperature with the lumped heat capacitance and without evaporation model compares reasonably well with the experimental findings. The particles of diameter greater than 42 μm have both lower computed temperature and axial velocity than their respective test values. In the absence of gravity, the axial acceleration of a powder particle is inversely proportional to the square of the particle radius. The particle axial velocity should decrease with an increase in the particle

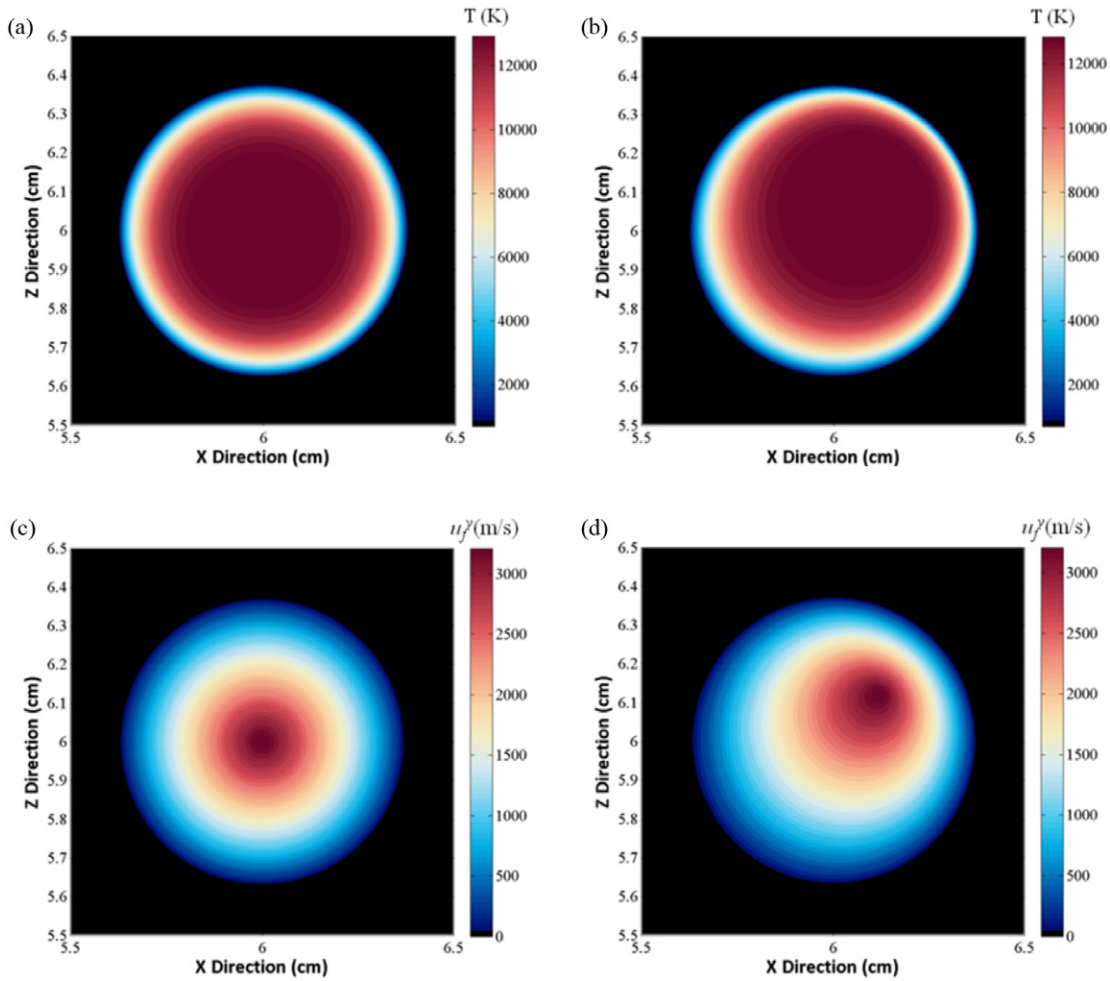

Figure 6. (*a*) Axisymmetric and (*b*) non-axisymmetric BCs of temperature; (*c*) axisymmetric and (*d*) non-axisymmetric BCs of velocity at the nozzle exit.

diameter. The axial velocity and the temperature of powder particles also depend on their trajectories in the 3D space since the temperature and the axial velocity of the plasma monotonically decrease in the axial and the radial directions.

The computed particle mean temperature and axial velocity for axisymmetric and non-axisymmetric BCs at the nozzle exit are compared in figure 10. The closeness to each other of the two results implies that the non-axisymmetry in the BCs has no significant effect on particles' temperature and axial velocity. In figure 10, the simulation results with the axisymmetric BCs and the fine mesh shown in figure 2(*d*) are compared with those obtained using the coarse mesh depicted in figure 2(*c*). It is clear that the coarse mesh has enough resolution to adequately capture the particulate behaviours.

5.4. Effects of turbulence modulation on plasma flow with particle injection

We first consider the case when only carrier gas is injected into the plasma jet and then when both powder particles and the carrier gas are simultaneously injected. Results are computed both with and without considering effects of turbulence modulation.

The carrier gas is injected at a steady rate of 5 slm for $t > 3.5$ ms after the plasma jet has reached a steady state in 3.5 ms. The computed temperature and axial velocity fields at the mid-plane ABCD at $t = 6$ ms both with and without modelling the carrier gas injection are compared in figure 11. The temperature and velocity fields with and without the carrier gas injection are noticeably different near the injector nozzle exit as the injection of the carrier gas moves downwards the plasma near the point of injection. One can also conclude from results shown in figure 11 that regions of high temperature and axial velocity are slightly narrower when the injection of the carrier gas is considered than those when it is not considered. The plasma spreads less in the radial direction with the consideration of the carrier gas flow.

The 3D trajectories of three different groups of particles and their distributions on the substrate are computed with and without considering the carrier gas flow. For $t = 18$ ms, these are shown in figure 12. These plots reveal that particles are more dispersed and located lower on the substrate with the consideration of the carrier gas flow than those without considering the carrier gas flow. The carrier gas

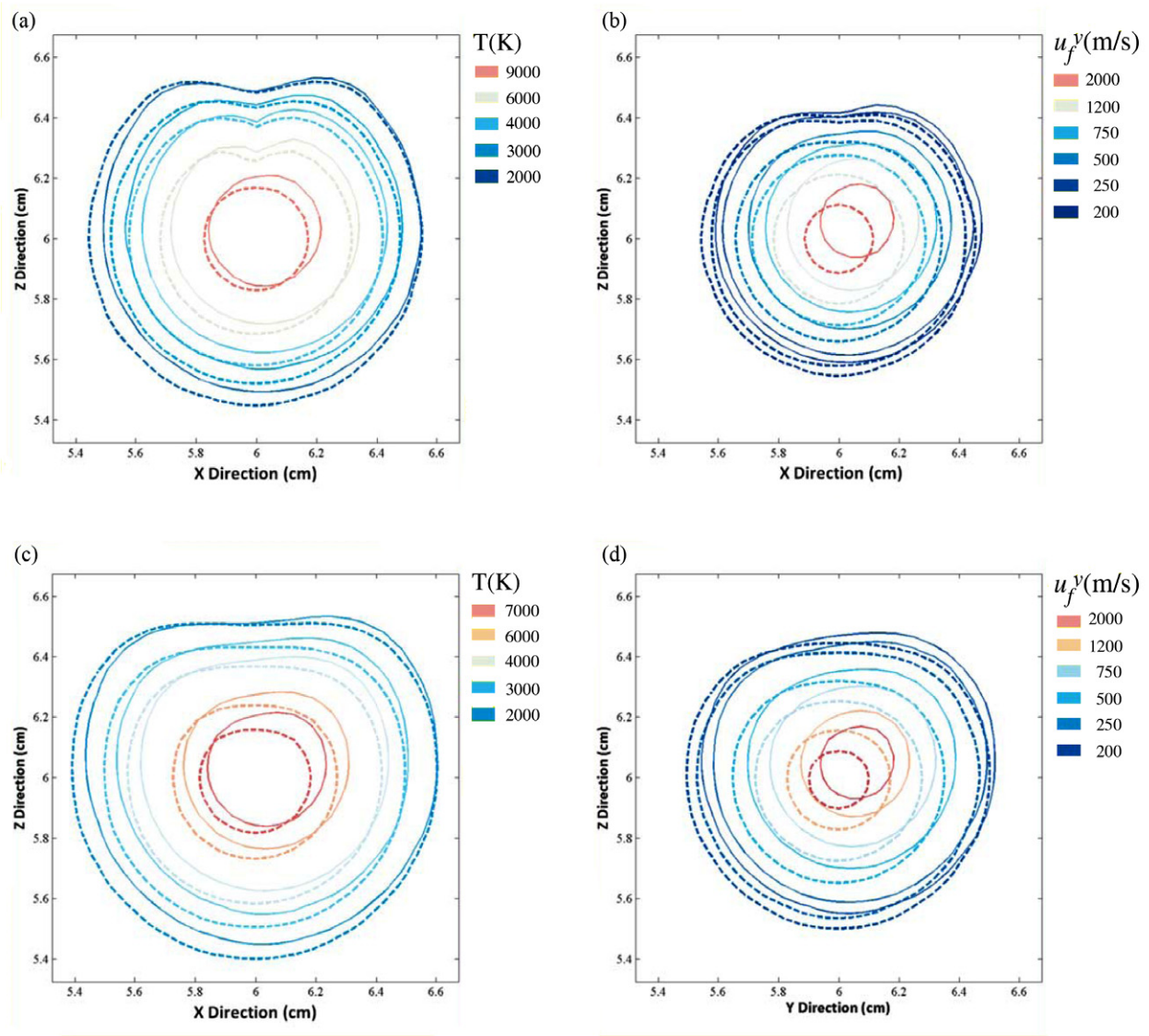

Figure 7. Contours of (*a*) temperature and (*b*) axial velocity at $Y = 0.6$ cm, (*c*) temperature and (*d*) axial velocity at $Y = 0.9$ cm under axisymmetric (dashed curves) and non-axisymmetric (solid curves) BCs at the nozzle exit.

changed the plasma temperature and velocity, as well as the particle trajectory. The particle mean axial velocity and the temperature calculated without and with the consideration of the carrier gas flow are compared in figure 13. Due to the injection of the carrier gas, the mean axial velocity and the temperature of particles are decreased.

We have computed results with and without turbulence modulation to evaluate effects on both the plasma jet and the particles characteristics. As listed in equation (26) the particle volume fraction α_k influences the source terms S_{pk} and $S_{p\varepsilon}$. In order to obtain realistic results and draw reliable conclusions when considering turbulence modulation, sufficiently large number of computational particles must be injected into the plasma. Results presented herein are at $t = 18$ ms with the maximum number of computational particles that had reached the substrate for $3.5 < t < 18$ ms equal to 12 693 with and 12 734 without considering turbulence modulation.

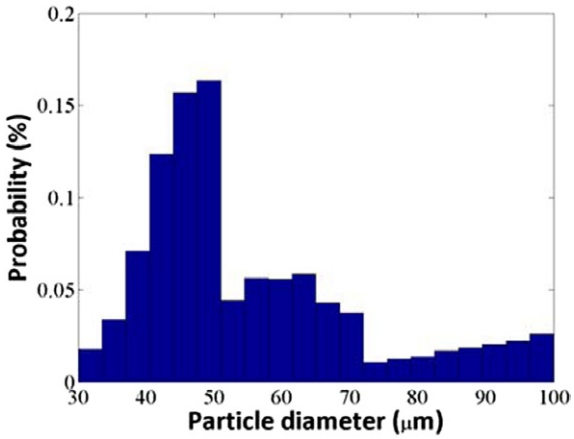

Figure 8. ZrO_2 particle size distribution.

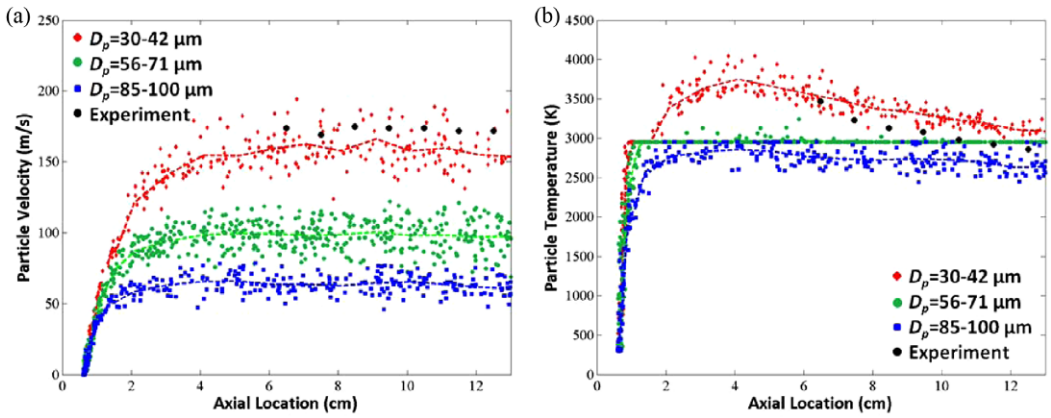

Figure 9. Comparison of the computed and the experimental values of (*a*) the axial velocity and (*b*) the temperature of powder particles (dashed curves pass through the mean values) for the axisymmetric BCs at the nozzle exit.

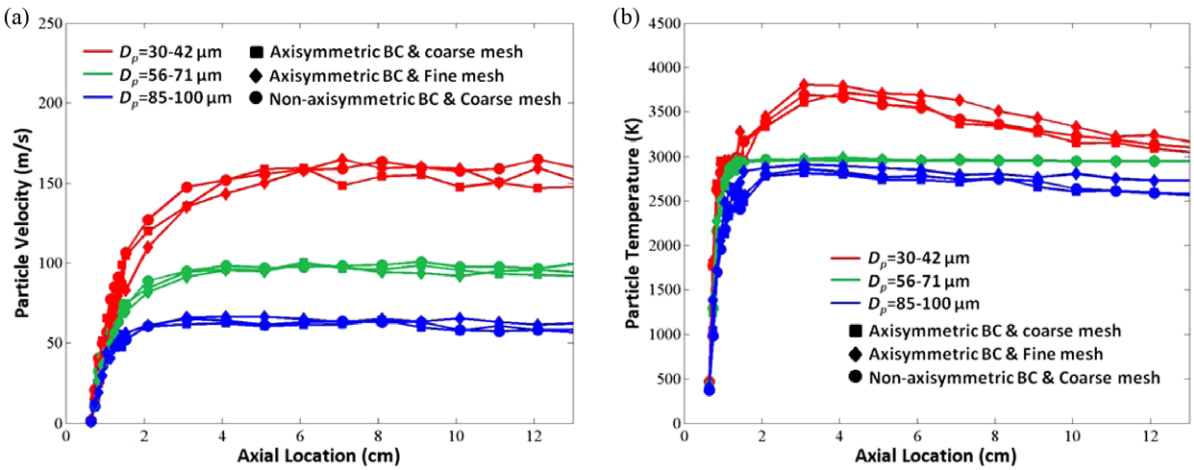

Figure 10. Comparison of the computed axial velocity and temperature of powder particles for axisymmetric and non-axisymmetric BCs at the nozzle exit and for the fine and coarse meshes, $t = 18$ ms.

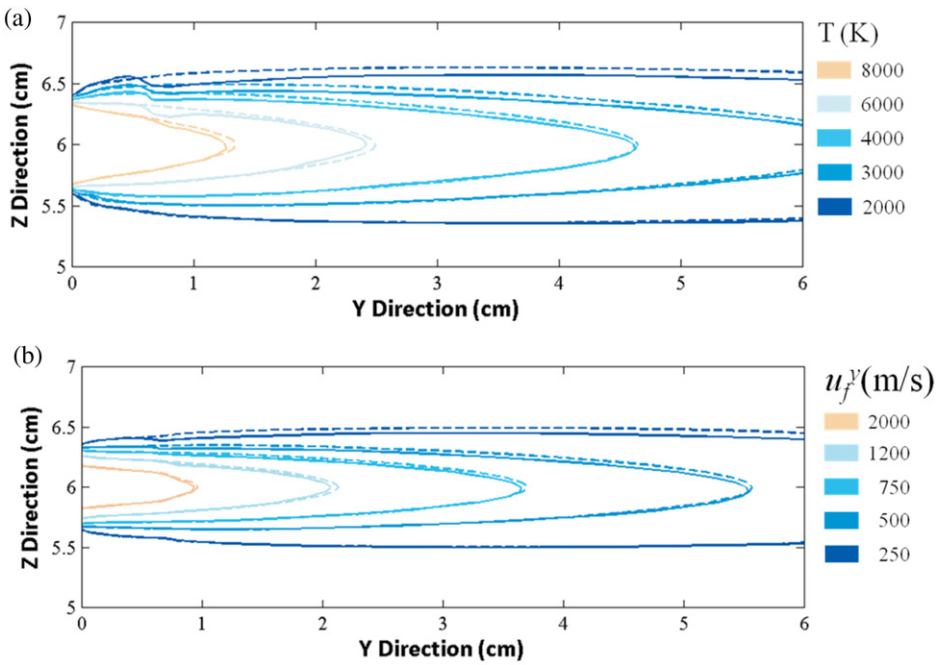

Figure 11. On the mid-plane, contours of (*a*) the temperature and (*b*) the axial velocity with (solid curves) and without (dashed curves) carrier gas injection.

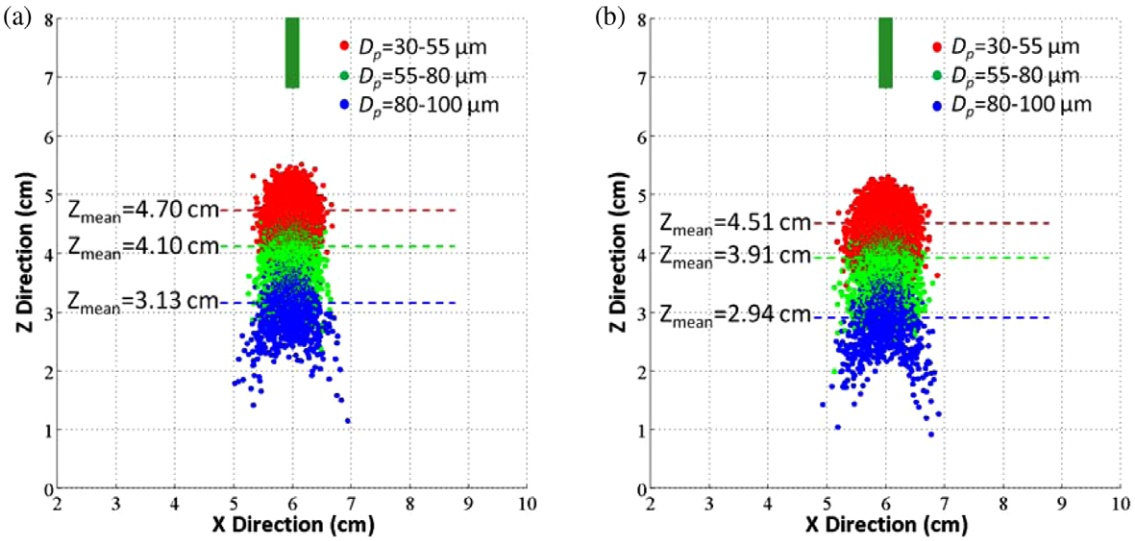

Figure 12. Particle distributions on the substrate (*a*) without, and (*b*) with the consideration of the carrier gas flow.

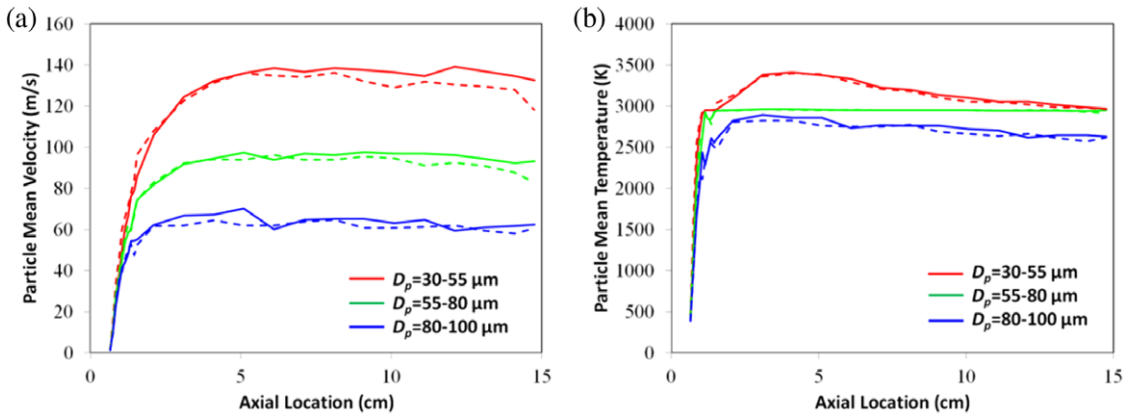

Figure 13. Comparison of the particle mean (*a*) axial velocity, and (*b*) temperature with (dashed line) and without (solid lines) the consideration of the carrier gas flow.

In figure 14 we have compared the turbulent kinetic energy and its dissipation rate within a small region of the mid-plane computed with and without considering turbulence modulation. The percentage reduction in the turbulent kinetic energy, d_k, and the dissipation rate, d_ε, are defined as $d_k = 100\left(k_{w/o} - k_w\right)/k_{w/o}$ and $d_\varepsilon = 100(\varepsilon_{w/o} - \varepsilon_w)/\varepsilon_{w/o}$, where subscripts w/o and w denote, respectively, values of the variable computed without and with the consideration of turbulence modulation. Positive values of d_k and d_ε indicate the relative reduction in the turbulent kinetic energy and the dissipation rate, respectively. As should be clear from results depicted in figures 14(*c*), (*f*) and (*g*), the consideration of turbulence modulation reduces the turbulent kinetic energy and its dissipation rate by more than 30% and 40% , respectively, in regions where particles are concentrated. In order to show the 3D effect of the turbulence modulation, variations of $k_{w/o}$, k_w, $\varepsilon_{w/o}$ and ε_w in the radial direction, and contour plots of the percentage reduction within the zone of interest (ZOI) at two different axial locations are exhibited in figures 15 and 16. At both locations the reductions in the turbulent kinetic energy and its dissipation rate exceed 15%. Although the effect of turbulence modulation on plasma turbulent kinetic energy and its dissipation rate are notable, the variations of the plasma temperature and the axial velocity are very small as shown in figure 17.

Even when identical particles are injected through the powder port, they will have different trajectories and traverse through different regions of the plasma jet because the velocity fluctuation $\boldsymbol{u}'$ is randomly assigned through a Gaussian distribution. It is thus very arduous task to study the turbulence modulation effect on two identical particles due to the randomness in $\boldsymbol{u}'$. Thus, only statistical information of particles can be utilized to draw reasonable conclusions. The particle distributions on the substrate with and without considering turbulence modulation are plotted in figures 18(*a*) and (*b*). The temperature and velocity distributions are plotted in figures 18(*c*) and (*d*) within the ZOI 1 cm × 2.5 cm located at ($X = 6$ cm, $Z = 3.75$ cm). The contours are plotted by interpolating values of parameters for the individual particles.

In figure 19, the probabilities of temperature and axial velocity of all particles having given values of the temperature

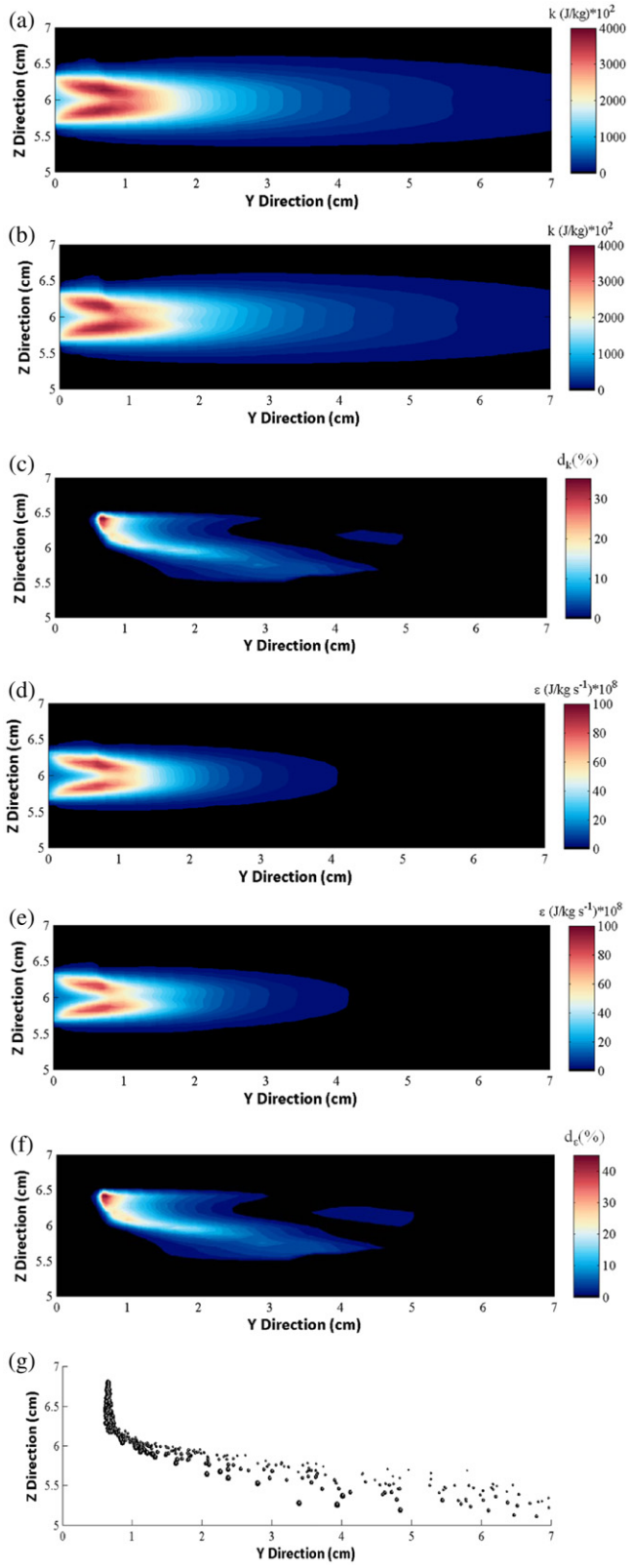

Figure 14. Fringe plots of the turbulent kinetic energy (*a*) without and (*b*) with the consideration of turbulence modulation, (*c*) difference in the turbulent kinetic energy for cases (*a*) and (*b*); the rate of turbulence kinetic energy (*d*) without and (*e*) with turbulence modulation, (*f*) difference in the rate of turbulence kinetic energy for cases (*d*) and (*e*); (*g*) particle distribution at the mid-plane $X = 6$ cm (size of a particle is magnified 400 times).

and the axial velocity are compared with and without considering turbulence modulation for three different particle sizes $d_p = 30$–$55\,\mu$m, 55–80 μm and 80–100 μm, labelled as groups 1, 2 and 3, respectively. The mean and the standard deviation of the particle temperature and the axial velocity are listed in table 5. Results are compared by listing the differences, $d = (\phi_{\mathrm{w}} - \phi_{\mathrm{w/o}}) \times 100/\phi_{\mathrm{w/o}}$, where subscripts w and w/o denote the particle characteristic when it reaches the substrate computed with and without turbulence modulation. From the summary of results provided in table 5, we conclude that the influence of turbulence modulation on the mean values of particles' temperature and axial velocity is small. The mean values of particles' temperature and axial velocity increase with an increase in the turbulence modulation for all three groups of particles. The larger value of the standard deviation indicates a wider distribution. For group 1, the temperature and the velocity distributions are narrower than those for groups 2 and 3.

In figure 20 we have plotted probabilities of the X- and the Z-coordinates of particles when they strike the substrate, and have listed in table 6 the mean and the standard deviations of these values. From values listed in table 6, we conclude that the influence of turbulence modulation on the mean value of particles' X-coordinate is small. However, there is notable difference between $Z^{\mathrm{w}}_{\mathrm{mean}}$ and $Z^{\mathrm{w/o}}_{\mathrm{mean}}$ for the three groups of particles, and particles' Z-coordinate moves up with the consideration of the turbulence modulation. This relative displacement in the Z-direction increases with an increase in the particles' diameter.

6. Conclusions

We have studied the effect of turbulence modulation on three-dimensional (3D) trajectories of powder particles injected with the carrier gas normal to the dominant plasma flow direction. The interactions among the particles, the carrier gas and the plasma make the plasma flow non-axisymmetric about the nozzle axis and necessitate the analysis of the 3D problem. The standard method of turbulence modulation has been adopted in this work. It is found that the consideration of turbulence modulation segregates particles striking the substrate into different locations depending on their mean diameters, and noticeably affects the turbulence kinetic energy. However, the mean temperatures and the mean axial velocity of particles are not influenced much by the turbulence modulation. We note that the particle volume fraction, the Reynolds number, the drag coefficient, the viscosity, the turbulent kinetic energy and its dissipation rate, and the relative velocity between a particle and the plasma in equations (26)–(29) vary from point to point in the computational domain. It is hard to ascertain the effect of each parameter on turbulence modulation directly from the equations even after the variables have been non-dimensionalized. In order to ascertain these effects, a comprehensive parametric study based on numerical simulations needs to be carried out and is left for a future work. Also the heat conduction within a particle, the particle melting

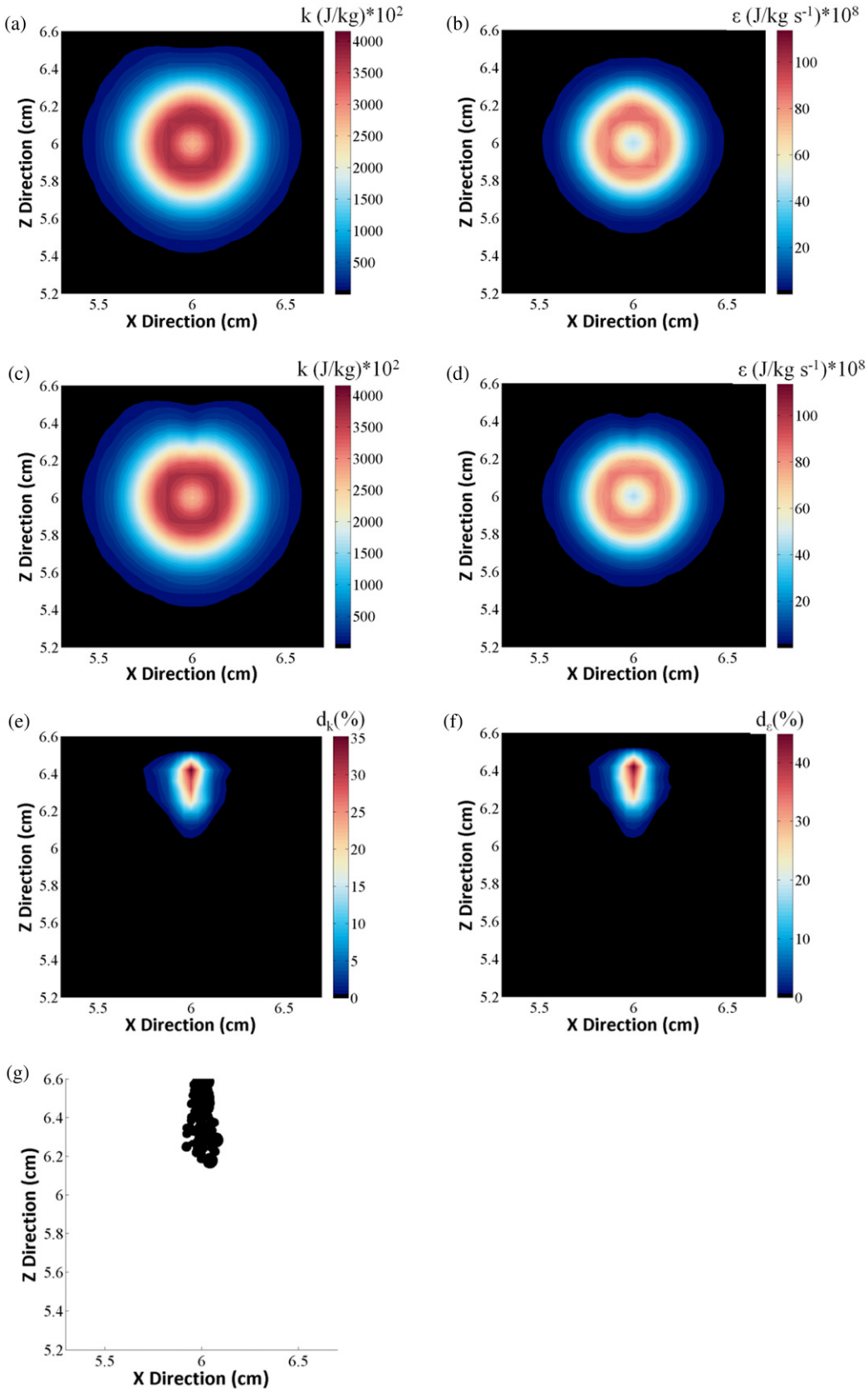

Figure 15. Fringe plots of the turbulent kinetic energy (*a*) without and (*b*) with the consideration of turbulence modulation, (*c*) difference in the turbulent kinetic energy for cases (*a*) and (*b*); turbulent dissipation rate (*d*) without and (*e*) with turbulence modulation, (*f*) difference in the turbulent dissipation rate for cases (*d*) and (*e*); (*g*) particle distribution at $Y = 0.64$ cm (size of a particle is magnified 400 times).

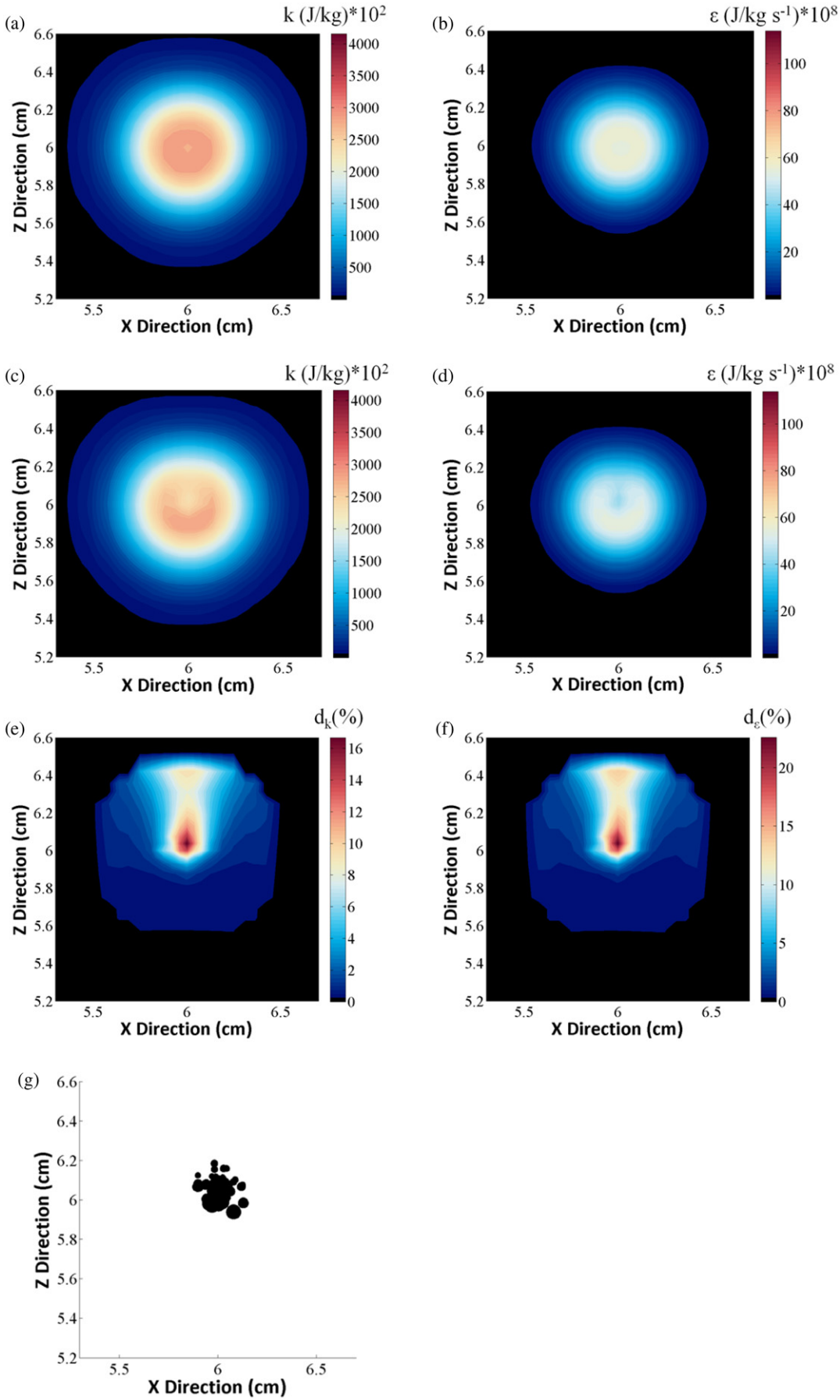

Figure 16. Fringe plots of the turbulent kinetic energy (*a*) without and (*b*) with the consideration of turbulence modulation, (*c*) difference between turbulent kinetic energies for cases (*a*) and (*b*); dissipation rate of turbulence kinetic energy (*d*) without and (*e*) with turbulence modulation, (*f*) difference between dissipation rates of turbulence kinetic energy for cases (*e*) and (*f*), (*g*) particle distribution at $Y = 0.9$ cm (size of a particle is magnified 400 times).

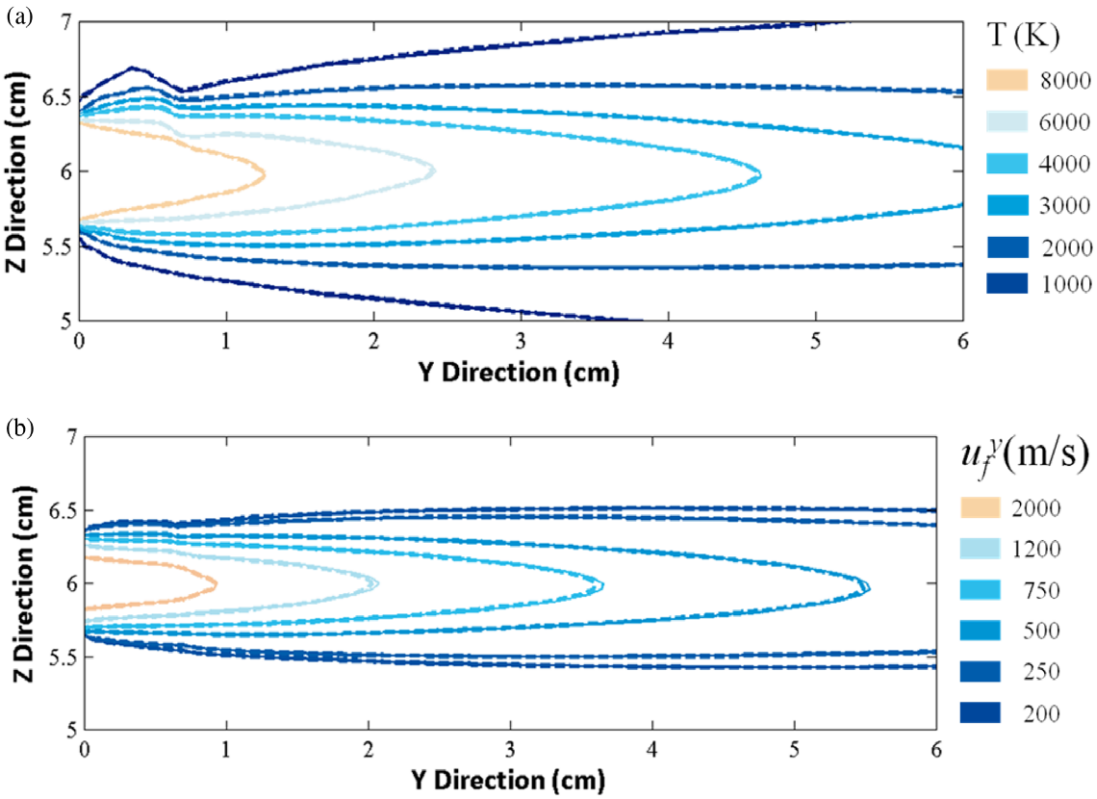

Figure 17. On the mid-plane, contour plots of the (*a*) temperature and (*b*) the axial velocity with (solid line) and without (dashed line) the consideration of turbulence modulation.

and likely evaporation of the material should be included to improve upon predictions from the model.

Appendix A. Supplementary equations

The diffusional mass flux, $\boldsymbol{J}_i$, of species i is given by

$$\boldsymbol{J}_i = -\frac{pM_i(D_i + D_\mathrm{t})}{R_\mathrm{g}T_f}\nabla\left(\frac{p_i}{p}\right) + \frac{\rho_i}{\rho}\sum_{j\neq e}\frac{pM_i(D_j + D_\mathrm{t})}{R_\mathrm{g}T_f}\nabla\left(\frac{p_i}{p}\right) + \boldsymbol{A}_i \tag{A1}$$

$$\boldsymbol{A}_i = \frac{1}{R_\mathrm{g}T_f}\left(M_i q_i \rho_i (D_i + D_\mathrm{t}) - \frac{\rho_i}{\rho}\sum_{j\neq e} M_j q_j \rho_j (D_j + D_\mathrm{t})\right) \times \frac{\nabla\rho_e}{q_e\rho_e} \tag{A2}$$

where subscript e denotes the quantity for a free electron, D_i is the laminar effective binary diffusivity of species i, $D_\mathrm{t} = \mu_\mathrm{t}/(\rho\, Sc_\mathrm{t})$ is the turbulent diffusivity, μ_t is the turbulent viscosity, Sc_t is the turbulent Schmidt number, p_i is the partial pressure of species i, p is the total pressure, $\boldsymbol{A}_i$ is the ambipolar forced diffusion flux, q_i is the electric charge per unit mass of species i,and a repeated index is not summed.

The viscous stress tensor, $\boldsymbol{\sigma}$, is given by

$$\boldsymbol{\sigma} = (\mu + \mu_\mathrm{t})\left[\nabla\boldsymbol{u}_f + (\nabla\boldsymbol{u}_f)^\mathrm{T}\right] + (\lambda + \lambda_\mathrm{t})(\nabla\cdot\boldsymbol{u}_f)\boldsymbol{I} \tag{A3}$$

where μ is the molecular viscosity, λ is the second viscosity, $\lambda_\mathrm{t} = -(2/3)\mu_\mathrm{t}$, and $\boldsymbol{I}$ is the identity tensor.

The heat flux vector, $\boldsymbol{q}$, is given by

$$\boldsymbol{q} = -\left(K_h + \frac{c_{ph}\mu_\mathrm{t}}{Pr_\mathrm{t}}\right)\nabla T_f + \sum_i h_i \boldsymbol{J}_i \tag{A4}$$

where K_h is the laminar thermal conductivity, c_{ph} is the mixture specific heat at constant pressure and Pr_t is the turbulent Prandtl number.

The turbulence production, ϕ, due to viscous effects is given by

$$\phi = \mu_\mathrm{t}\left[\nabla\boldsymbol{u}_f\cdot(\nabla\boldsymbol{u}_f + \nabla\boldsymbol{u}_f^\mathrm{T}) - \frac{2}{3}(\nabla\cdot\boldsymbol{u}_f)^2\right]. \tag{A5}$$

Appendix B. Chemical reactions

The chemical reactions considered among the species Ar, Ar^+, H_2, H_2^+, N_2, N_2^+, N, N^+, O_2, O, O^+ and $e^-$are listed below. These have been incorporated in the software LAVA-3DI

Dissociation (*kinetic reactions*):

$$H_2 + M = 2H + M \tag{B1}$$

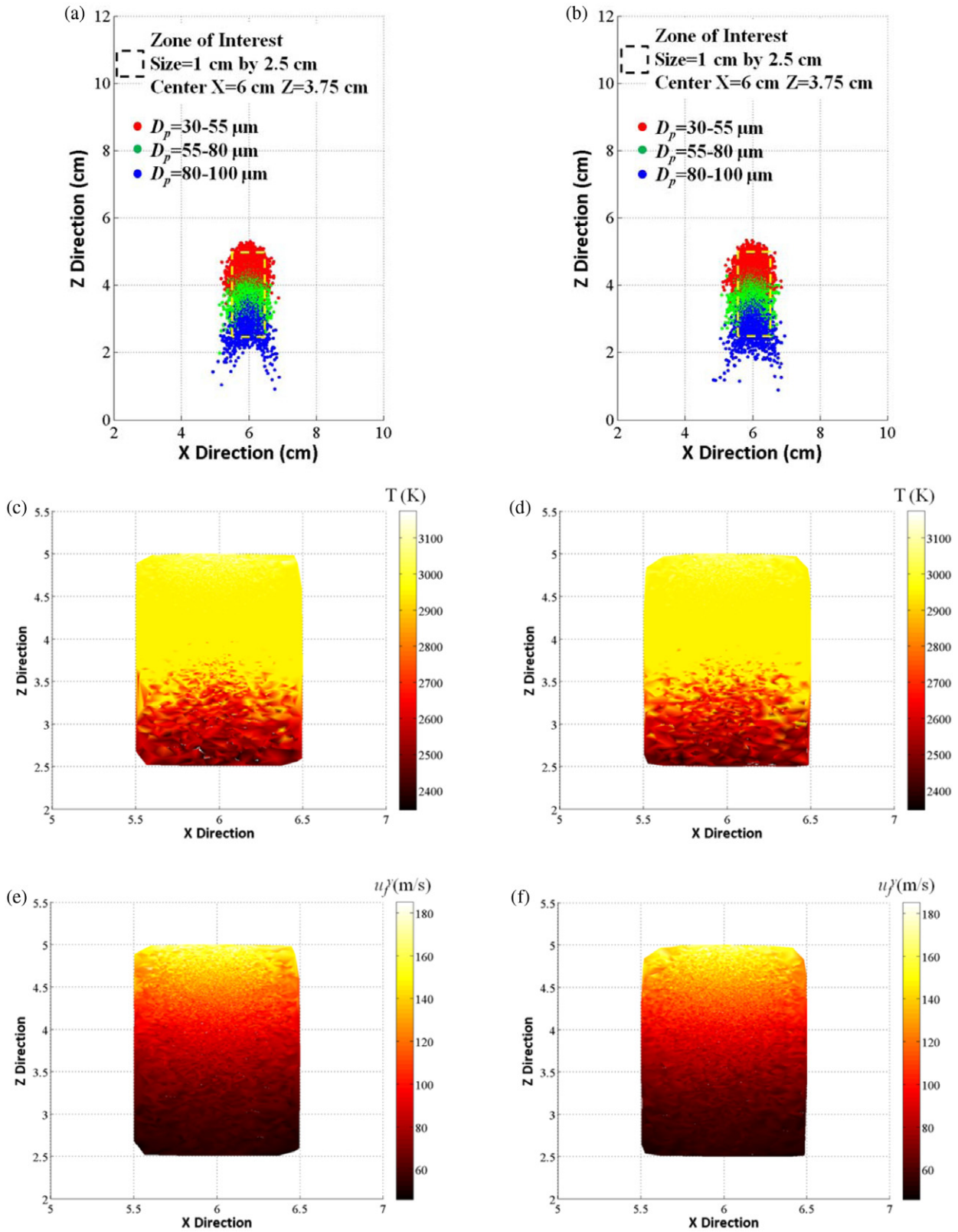

Figure 18. Particle distributions on the substrate (*a*) with and (*b*) without considering turbulence modulation; particle temperature (*c*) with and (*d*) without considering turbulence modulation; particle axial velocity (*e*) with and (*f*) without considering turbulence modulation.

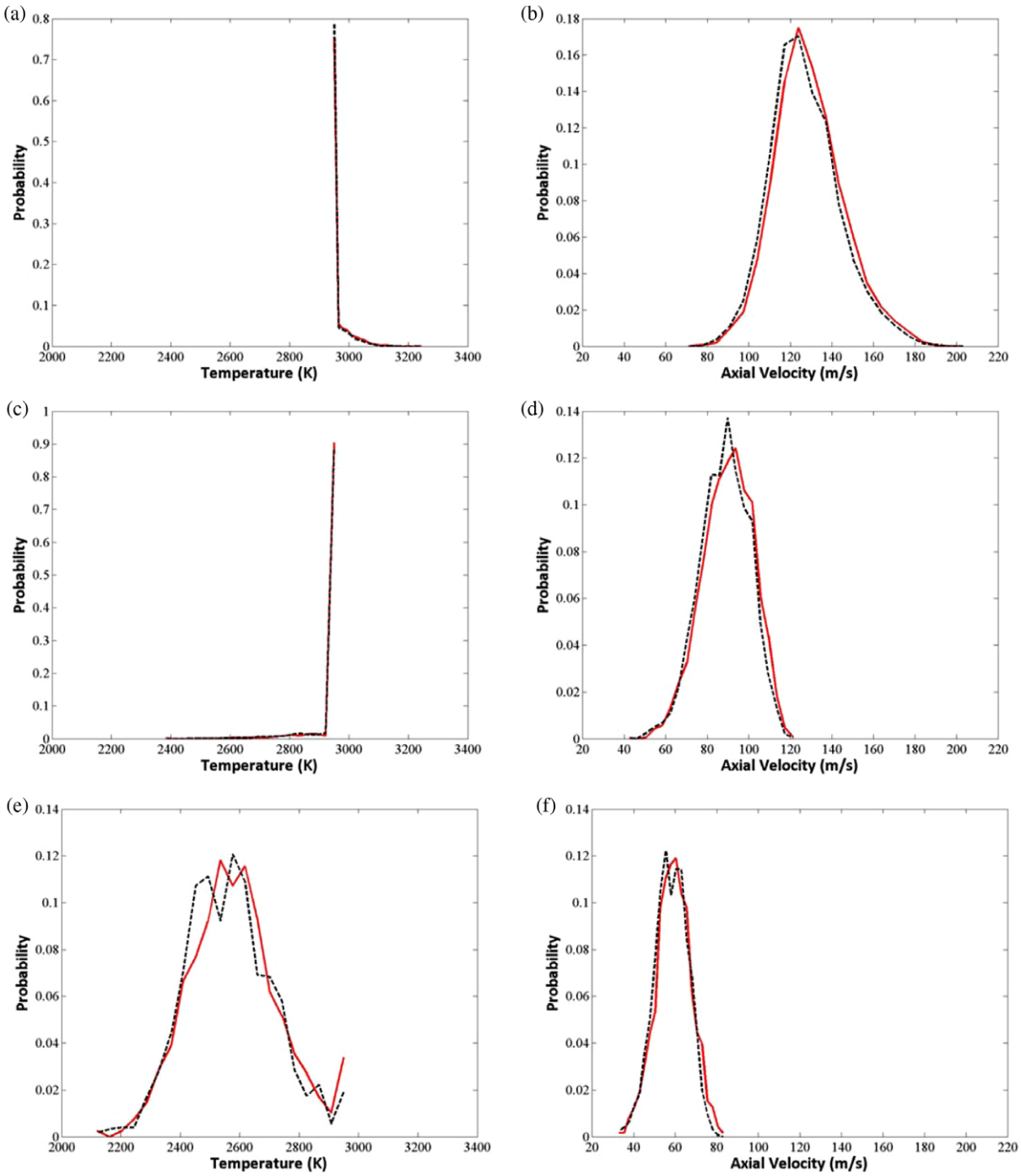

Figure 19. Probabilities of particle temperature (left) and axial velocity (right) with (solid line) and without (dashed line) considering turbulence modulation: d_p = (*a*) 30–55 μm, (*b*) 55–80 μm and (*c*) 80–100 μm.

$$N_2 + M = 2N + M \quad \text{(B2)}$$

$$O_2 + M = 2O + M \quad \text{(B3)}$$

where M is the third body defined in [57].

Electron impact and associative ionization (*equilibrium reactions*):

$$Ar + e^- = Ar^+ + 2e^- \quad \text{(B4)}$$

$$H + e^- = H^+ + 2e^- \quad \text{(B5)}$$

$$N + e^- = N^+ + 2e^- \quad \text{(B6)}$$

$$O + e^- = O^+ + 2e^- \quad \text{(B7)}$$

$$N + N = N_2^+ + e^-. \quad \text{(B8)}$$

Charge exchange reactions (*equilibrium reactions*):

$$N_2 + N^+ = N_2^+ + N. \quad \text{(B9)}$$

Table 5. Comparison of statistics of particles' temperature and axial velocity when they reach the substrate with and without considering turbulence modulation.

Diameter (μm)		No of particles	T_{mean} (K)	T_{std} (K)	V_{mean} (m s^{-1})	V_{std} (m s^{-1})
	w	8183	2964	31.9	129.2	16.9
d_p 30–55	w/o	8190	2961	32.5	127.2	16.6
	d (%)		0.1	−1.8	1.6	1.8
	w	3366	2936	52.8	89.9	12.2
d_p 55–80	w/o	3244	2934	55.3	88.5	11.9
	d (%)		0.1	−4.5	1.6	2.5
	w	1185	2584	154.2	59.2	8.4
d_p 80–100	w/o	1259	2567	148.1	58.2	8.0
	d (%)		0.7	4.1	1.7	5.0

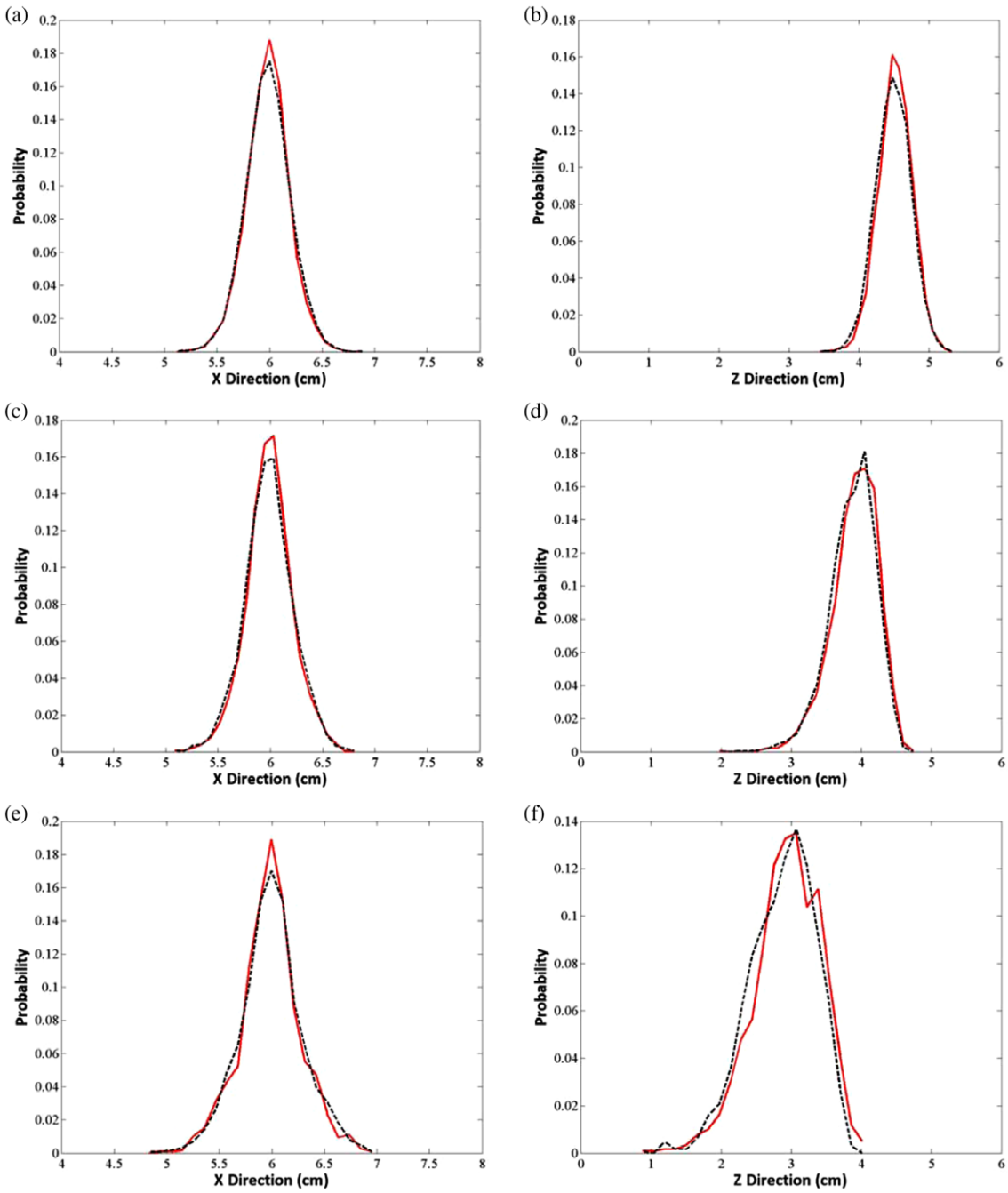

Figure 20. Probabilities of particle locations on the X- (left figure) and the Z- (right figure) axes with (solid line) and without (dashed line) considering turbulence modulation; $d_p =$ (*a*) 30–55 μm, (*b*) 55–80 μm and (*c*) 80–100 μm.

Table 6. Comparison of statistics of particles' dispersion on the substrate with and without considering turbulence modulation.

Diameter (μm)		No of particles	X_{mean} (cm)	X_{std} (cm)	Z_{mean} (cm)	Z_{std} (cm)
	w	8183	5.98	0.22	4.52	0.24
d_p 30–55	w/o	8190	5.98	0.23	4.49	0.25
	d (%)		0.0	−4.3	0.7	−4.0
	w	3366	5.99	0.22	3.91	0.33
d_p 55–80	w/o	3244	5.98	0.23	3.87	0.33
	d (%)		0.2	−4.3	1.0	0.0
	w	1185	5.99	0.28	2.94	0.48
d_p 80–100	w/o	1259	5.99	0.29	2.8	0.47
	d (%)		0.0	−3.4	5.0	2.1

Molecular reactions (*equilibrium reactions*):

$$H + O_2 = OH + O \quad \text{(B10)}$$

$$H_2 + O = OH + H \quad \text{(B11)}$$

$$H_2O + O = 2OH \quad \text{(B12)}$$

$$H_2 + OH = H_2O + H. \quad \text{(B13)}$$

Acknowledgments

Shen Shang's work was partially supported by a grant from the Commonwealth Center of Advanced Manufacturing (CCAM) to Virginia Polytechnic Institute and State University. The authors are grateful to other team members, Drs Gary Pickrell, Ray Sinatra, Ann Bolcavage, Dave Rickerby and Mr Taylor Blair. We gratefully acknowledge receiving the source code for LAVA-P from the Idaho National Engineering and Environmental Laboratory.

References

[1] Lugscheider E and Weber T 1990 *IEEE Trans. Plasma Sci.* **18** 968
[2] Singh H, Sidhu B S, Puri D and Prakash S 2007 *Mater. Corros.* **58** 92
[3] Pfender E 1988 *Surf. Coat. Technol.* **34** 1
[4] Ramakrishnan S, Stokes A and Lowke J 1978 *J. Phys. D: Appl. Phys.* **11** 2267
[5] Planche M P, Coudert J F and Fauchais P 1998 *Plasma Chem. Plasma Process.* **18** 263
[6] Duan Z and Heberlein J 2002 *J. Therm. Spray Technol.* **11** 44
[7] Chazelas C, Coudert J F and Fauchais R 2005 *IEEE Trans. Plasma Sci.* **33** 416
[8] Nogues E, Vardelle M, Fauchais P and Granger P 2008 *Surf. Coat. Technol.* **202** 4387
[9] Selvan B, Ramachandran K, Sreekumar K P, Thiyagarajan T K and Ananthapadmanabhan P V 2009 *Vacuum* **84** 444
[10] Selvan B and Ramachandran K 2009 *J. Therm. Spray Technol.* **18** 846
[11] Lebouvier A, Delalondre C, Fresnet F, Boch V, Rohani V, Cauneau F and Fulcheri L 2011 *IEEE Trans. Plasma Sci.* **39** 1889
[12] Huang R Z, Fukanuma H, Uesugi Y and Tanaka Y 2013 *J. Therm. Spray Technol.* **22** 183
[13] Li H P and Pfender E 2007 *J. Therm. Spray Technol.* **16** 245
[14] Trelles J P, Pfender E and Heberlein J V R 2008 *IEEE Trans. Plasma Sci.* **36** 1026
[15] Trelles J P 2013 *J. Phys. D: Appl. Phys.* **46** 255201
[16] Selvan B, Ramachandran K, Pillai B C and Subhakar D 2011 *J. Therm. Spray Technol.* **20** 534
[17] Mariaux G and Vardelle A 2005 *Int. J. Therm. Sci.* **44** 357
[18] Qunbo F, Lu W and Fuchi W 2005 *J. Mater. Process. Technol.* **166** 224
[19] Chang C H and Ramshaw J D 1994 *Phys. Plasmas* **1** 3698
[20] Ramshaw J D and Chang C H 1992 *Plasma Chem. Plasma Process.* **12** 299
[21] Pfender E and Lee Y C 1985 *Plasma Chem. Plasma Process.* **5** 211
[22] Lee Y C, Chyou Y P and Pfender E 1985 *Plasma Chem. Plasma Process.* **5** 391
[23] Wan Y P, Prasad V, Wang G X, Sampath S and Fincke J R 1999 *Trans. ASME* C **121** 691
[24] Chen X and Pfender E 1983 *Plasma Chem. Plasma Process.* **3** 351
[25] Westhoff R, Trapaga G and Szekely J 1992 *Metall. Trans.* B **23** 683
[26] Pfender E 1994 *Thin Solid Films* **238** 228
[27] Williamson R L, Fincke J R and Chang C H 2000 *Plasma Chem. Plasma Process.* **20** 299
[28] Wan Y P, Gupta V, Deng Q, Sampath S, Prasad V, Williamson R and Fincke J R 2001 *J. Therm. Spray Technol.* **10** 382
[29] Williamson R L, Fincke J R, Crawford D M, Snyder S C, Swank W D and Haggard D C 2003 *Int. J. Heat Mass Transfer* **46** 4215
[30] Njah Z, Mostaghimi J, Faghri M and Boulos M 1993 *Int. J. Heat Mass Transfer* **36** 3897
[31] Vardelle A, Fauchais P, Dussoubs B and Themelis N J 1998 *Plasma Chem. Plasma Process.* **18** 551
[32] Ahmed I and Bergman T 2001 *J. Heat Transfer* **123** 188
[33] Li H P and Chen X 2001 *Thin Solid Films* **390** 175
[34] Dussoubs B, Vardelle A, Mariaux G, Themelis N and Fauchais P 2001 *J. Therm. Spray Technol.* **10** 105
[35] Ramachandran K and Nishiyama H 2002 *J. Phys. D: Appl. Phys.* **35** 307
[36] Li H P and Chen X 2002 *Plasma Chem. Plasma Process.* **22** 27
[37] Mariaux G, Legros E and Vardelle A 2003 *Int. Thermal Spray Conf. 2003: Advancing the Science and Applying the Technology (Orlando, FL)*
[38] Ramachandran K and Nishiyama H 2004 *Thin Solid Films* **457** 158
[39] Xiong H-B, Zheng L-L, Sampath S, Williamson R L and Fincke J R 2004 *Int. J. Heat Mass Transfer* **47** 5189
[40] Khelfi D, El-Hadj A A and Aït-Messaoudène N 2008 *Rev. Energies Renouvelables CISM (Oum el Bouaghi, Algeria)*
[41] Meillot E and Balmigere G 2008 *Surf. Coat. Technol.* **202** 4465
[42] Wang F C, Fan Q B, Wang L, Wang Q S and Ma Z 2009 *Adv. Mater. Res.* **75** 1
[43] Gore R A and Crowe C T 1989 *Int. J. Multiphase Flow* **15** 279
[44] Hetsroni G 1989 *Int. J. Multiphase Flow* **15** 735
[45] Yuan Z and Michaelides E E 1992 *Int. J. Multiphase Flow* **18** 779

[46] Elghobashi S 1994 *Appl. Sci. Res.* **52** 309
[47] Crowe C T, Troutt T R and Chung J N 1996 *Annu. Rev. Fluid Mech.* **28** 11
[48] Gouesbet G and Berlemont A 1999 *Prog. Energy Combust. Sci.* **25** 133
[49] Crowe C T 2000 *Int. J. Multiphase Flow* **26** 719
[50] Lain S and Sommerfeld M 2003 *Int. J. Heat Fluid Flow* **24** 616
[51] Lightstone M F and Hodgson S M 2004 *Can. J. Chem. Eng.* **82** 209
[52] Poelma C, Westerweel J and Ooms G 2007 *J. Fluid Mech.* **589** 315
[53] Balachandar S and Eaton J K 2010 *Annu. Rev. Fluid Mech.* **42** 111
[54] Gray S L 2012 Turbulence modulation of polydisperse particles in a square particle-laden jet: numerical investigation *Thesis* Virginia Polytechnic Institute and State University
[55] Fauchais P 2004 *J. Phys. D: Appl. Phys.* **37** 86
[56] Liu C-H F 1977 Numerical analysis of the anode region of high intensity arcs *Thesis* University of Minnesota
[57] Park J H, Pfender E and Chang C H 2000 *Plasma Chem. Plasma Process.* **20** 165
[58] Kai C and Xi C 2004 *J. Phys. D: Appl. Phys.* **37** 2385
[59] Xu D Y, Chen X and Pan W X 2005 *Int. J. Heat Mass Transfer* **48** 3253
[60] Delluc G, Perrin L, Ageorges H, Fauchais P and Pateyron B 2003 *Proc. 16th Int. Symp. on Plasma Chemistry ISPC16 (Bari, Italy)*
[61] Orourke P J 1989 *J. Comput. Phys.* **83** 345
[62] Vardelle M, Vardelle A, Fauchais P, Li K I, Dussoubs B and Themelis N J 2001 *J. Therm. Spray Technol.* **10** 267
[63] Elghobashi S 1991 *Appl. Sci. Res.* **48** 301
[64] Mando M, Lightstone M F, Rosendahl L, Yin C and Sorensen H 2009 *Int. J. Heat Fluid Flow* **30** 331
[65] Boulet P and Moissette S 2002 *Int. J. Heat Mass Transfer* **45** 4201
[66] Smith W, Jewett T, Sampath S, Swank W and Fincke J 1997 *Thermal Spray: A United Forum for Scientific and Technological Advances* (Materials Park, OH: ASM International)